A layer-specific model of cortical sensory aging

Peng Liu [1, 2, 3, 4] *, Juliane Doehler [1, 3] *, Julia U. Henschke [1, 3], Alicia Northall [1], Angela Serian [5], Dietrich S. Schwarzkopf [6, 7], Oliver Speck [3, 8, 9, 10] , Janelle M.P. Pakan [1, 3, 9], Esther Kuehn [1, 2, 4, 9]

1. Institute for Cognitive Neurology and Dementia Research (IKND), Otto-von-Guericke University Magdeburg, 39120 Magdeburg, Germany
2. Hertie Institute for Clinical Brain Research (HIH), 72076 Tübingen, Germany
3. German Centre for Neurodegenerative Diseases (DZNE), 39120 Magdeburg, Germany
4. German Centre for Neurodegenerative Diseases (DZNE), 72076 Tübingen, Germany
5. Institute of Cognitive and Clinical Neuroscience, Central Institute of Mental Health, Medical Faculty Mannheim, Ruprecht-Karls-University Heidelberg, 68159 Mannheim, Germany
6. School of Optometry & Vision Science, The University of Auckland, Auckland, New Zealand
7. Experimental Psychology, University College London, London, UK
8. Department of Biomedical Magnetic Resonance, Otto-von-Guericke University Magdeburg, 39120 Magdeburg, Germany
9. Centre for Behavioural Brain Sciences (CBBS) Magdeburg, 39106 Magdeburg, Germany
10. Leibniz Institute for Neurobiology, 39120 Magdeburg, Germany

* These authors contributed equally

Corresponding Author
Juliane Doehler, juliane.doehler@med.ovgu.de

Competing Interests
No competing interests to declare.

Acknowledgments

This project was funded by the German Research Foundation (Deutsche Forschungsgemeinschaft, DFG) (KU 3711/2-1, project number: 423633679 to E.K., Project-ID 425899996 - SFB 1436 to E.K and J.M.P.P., and project number 362321501 - RTG 2413 to J.M.P.P.).

We thank Elnaz Khosroshahi, Melina Trigoussis, Lilith-Sophie Lange, Anastasia Chrysidou, Johanna Nölle and Sophie Christine Busalt for their support in participant recruitment and data collection, and Ridhim Joshi and Cathleen Knape for technical assistance and data collection in mice.

Abstract

The segregation of processes into cortical layers is a convergent feature in animal evolution. However, it remains unclear how changes in the cortical layer architecture affect sensory system function and dysfunction. To address this, we conducted layer-specific in-vivo 7T-MRI of the primary somatosensory cortex in younger and older adults and in an adult with congenital arm loss. Input layer IV was enlarged and more myelinated in older adults, which drove extended sensory input signals, whereas with congenital arm loss, input layer IV contralateral to the missing limb had shrunk. Age-related cortical thinning was driven by deep layers, and accompanied by altered functional modulation and behavioral readouts. Neuronal calcium imaging and histology across aging mice revealed altered excitatory/inhibitory balance, with deep-layer cell loss and overall increased parvalbumin cell density as potential neural underpinnings. Therefore, the segregation of processes into cortical layers has a unique age-related profile.

Keywords

overactivation, plasticity, receptive fields, *in-vivo* myeloarchitecture, sensory deprivation

Introduction

Sensory processing is organized in a layered architecture with segregated input, output, and modulatory circuits. The layered architecture of sensory systems is a convergent feature in animal evolution[1]. A model on functional and dysfunctional sensory systems requires a detailed understanding of alterations in the layer-specific architecture and their associated phenotypes. Critically, this knowledge is so far lacking not only for sensory systems but for cortical dysfunction in general.

Sensory dysfunction has been associated with different cortical phenotypes, including functional overactivation[2,3,4], increases in receptive field sizes[3,5], decreases in lateral inhibition[3], and structural alterations such as cortical thinning[6]. However, it is unclear how changes in the cortical layer architecture may contribute to the specific functional and structural alterations that characterize sensory cortices with reduced functionality. Cortical aging serves as a suitable model system to investigate this question as structural and functional plasticity is observed at different levels of the processing hierarchy and affects behavior[2,3,4].

We tested four major hypotheses of how structural and functional alterations in the cortical layer architecture characterize cortical dysfunction. The 'preserved layer hypothesis' assumes that the structural layer architecture cannot be distinguished between younger and older adults with present methodology, motivated by the preserved layer architecture of primary motor cortex (MI) in older adults[7]. The 'altered input channel hypothesis' on the other hand assumes that age-related functional plasticity is characterized by a more or less pronounced input layer IV in older compared to younger adults. Previous studies have shown structural sensitivity of layer IV to sensory input statistics[8], which are higher in older adults due to increased age, but also weakened due to reduced peripheral nerve receptor density[9]. Our third, 'altered sensory modulation hypothesis' assumes that older compared to younger adults are characterized by a degradation of deep layers V and VI and/or superficial layers II and III, which mediates changes in the excitatory/inhibitory modulation of sensory inputs. In primates, deep layers of sensory cortex mediate inhibition[10,11], whereas in older adults, inhibition is assumed to be reduced[12]. Finally, the 'degraded border hypothesis' assumes that the low-myelin borders that exist inferior to the thumb representation[13], and occasionally between single finger representations[14], in input layer IV degrade with cortical aging and cause less precise functional representations[5].

To test these hypotheses, we employed a unique approach and acquired layer-specific structural and functional magnetic resonance imaging (fMRI) data using 7T-MRI of the primary somatosensory cortex (SI) of healthy younger and older adults together with behavioral assessments. We also investigated an individual with unilateral congenital arm loss to test for the effect of absent sensory input on the SI layer architecture. To better understand the mechanistic underpinnings, we analyzed younger and older mice using *in-vivo* two-photon calcium imaging and histological analyses (see **Fig. 1**). In humans, analyses were restricted to area 3b - the homologue of mouse SI[15]. This study inspires the investigation of cortical layers to reveal the fundamental mechanisms that underlie cortical dysfunction.

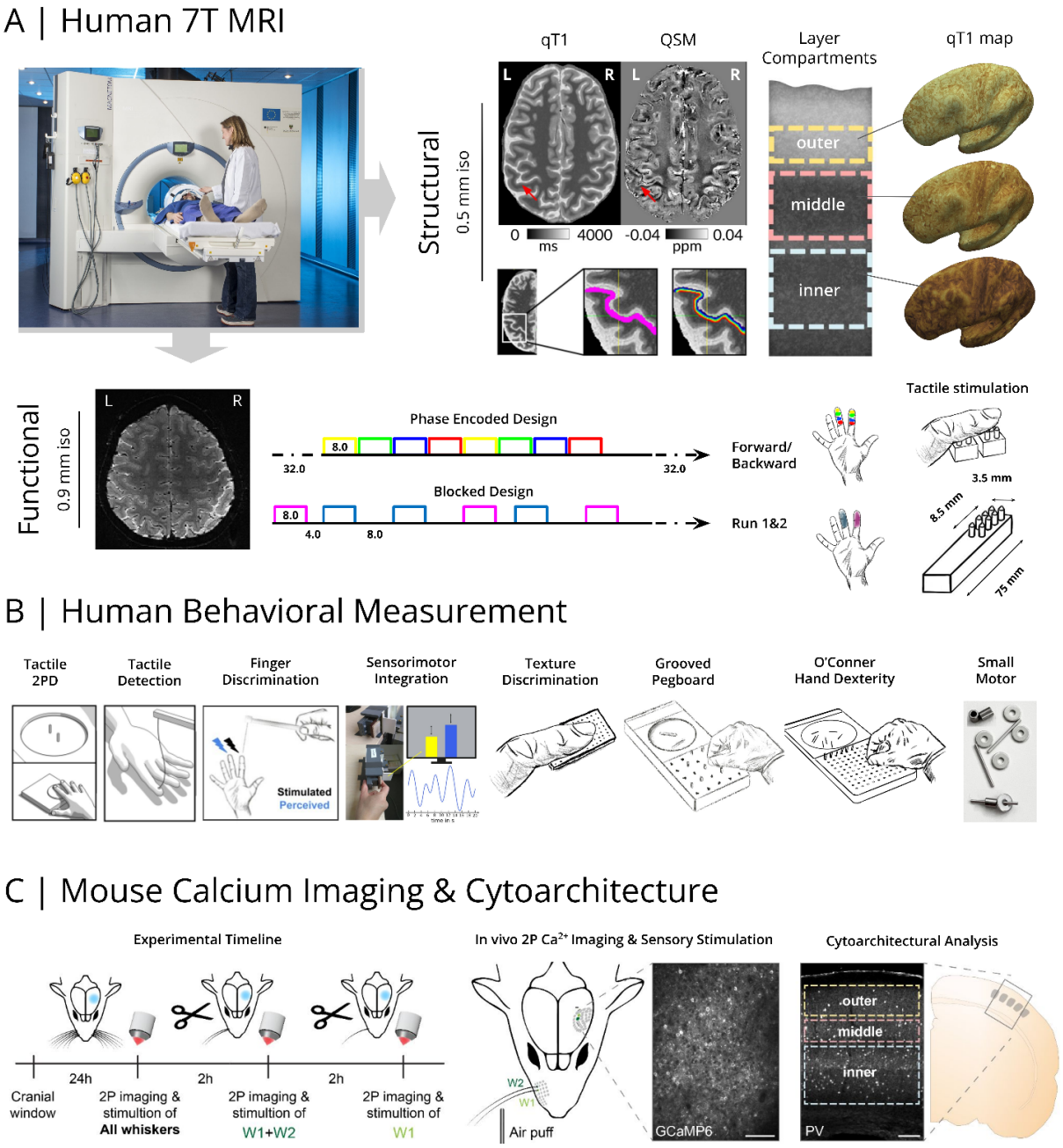

Figure 1. Overview Experimental Design (A) 7 Tesla Magnetic Resonance Imaging (7T-MRI) was used to investigate the layer-specific structural architecture of primary somatosensory cortex (SI) in younger and older adults using MP2RAGE and SWI data. MP2RAGE images were used to define SI layer compartments *in-vivo*. Red arrows indicate the region of interest (left BA3b hand area). Extracted qT1 and QSM values were mapped onto the individual's inflated, layer-specific cortical surface. Myelin staining was remodeled according to Dinse et al.[16]. 7T functional MRI (7T-fMRI) was used to investigate layer-specific functional changes in SI. Participants underwent several passive tactile stimulation paradigms in the scanner. Phase-encoded data were used for Fourier-based and population receptive field (pRF) analysis. **(B)** Younger and older adults underwent a behavioral test battery including tactile 2-point discrimination (2PD), tactile detection, finger discrimination, sensorimotor integration, texture discrimination, the Grooved Pegboard Test, the O'Connor Hand Dexterity Test and the Small Motor Test. (**C**) Barrel cortex two-photon calcium imaging (2PCI) of excitatory neurons expressing a genetically encoded calcium indicator (GCaMP6) during airpuff whisker stimulation: i) during baseline conditions with all whiskers, ii) after all whiskers were cut except two on the right-side (W1+W2; two-whisker condition), iii) after another whisker was cut leaving only one (W1; one-whisker condition). Post-mortem histological analysis examined underlying cytoarchitectural differences across cortical layers and aging. Scale bars 100 µm.

Results

Cortical thickness is layer-specific in older adults and with congenital hand loss

Our first hypothesis expects the structural layer architecture to be similar between younger and older adults ('preserved layer hypothesis'). According to this view, if cortical thinning occurs with aging, we expect homogenous thinning of all layers. To target this fundamental aspect of cortex organization, we analyzed structural and functional 7T MRI data of younger (n=20) and older (n=20) adults' SI (layer-specific structural study). SI layer definition followed a data-driven approach, assigning biological layers II and III to the outer compartment, input layer IV to the middle compartment, and layers V and VI to the inner compartment[17]. We localized individual finger representations using population receptive field (pRF) modeling (see **Fig. 1B**). In agreement with previous findings[17,18,19,20], the SI hand area was on average 2.01±0.10 mm thick (Mean±SD), but thinner in older compared to younger adults (older-younger=-0.1 mm; see **Table 1**)[3]. Critically, overall thinning was driven by reduced thickness of the inner compartment, whereas the outer and middle compartments were thicker in older compared to younger adults (see **Table 1, Fig. 2D, Table 1-supplemental table 1** for different localization approach**,** and **Table 1-supplemental table 2** for different layer compartmentalization scheme). While the thicker outer compartment may be driven by an outlier, the thicker middle compartment and the thinner inner compartment remain after removing the potential outlier (see **Fig. 2-supplemental figure 1**). This result of layer-specific cortical thinning and thickening in older adults' SI rejects the 'preserved layer hypothesis'.

hand area	All n = 40	**Younger** n = 20	**Older** n = 20	**Group Differences**			
	Mean ± SD	Mean ± SD	Mean ± SD	t	df	p_{perm}	CI_{perm}
total	2.01 ± 0.10	2.06 ± 0.07	1.95 ± 0.10	3.8	33.4	5.4^{-4} *	0.04, 0.17
outer	0.46 ± 0.06	0.41 ± 0.02	0.51 ± 0.04	-10.1	26.8	$< 2.2x10^{-16}$ *	-0.14, -0.07
middle	0.65 ± 0.10	0.56 ± 0.02	0.75 ± 0.04	-18.7	26.0	$< 2.2x10^{-16}$ *	-0.26, -0.13
inner	0.89 ± 0.21	1.10 ± 0.06	0.69 ± 0.04	26.6	31.0	$< 2.2x10^{-16}$ *	0.27, 0.54

Table 1. Layer-specific cortical thickness of the SI hand area. Shown are layer-specific (outer, middle, inner) mean cortical thickness values (Mean) and standard deviations (SD) in millimeters for the SI hand region (localized by vibro-tactile stimulation to the five fingertips of the right hand and population receptive field (pRF) mapping). Independent-samples random permutation Welch t-tests were calculated to investigate group differences (t=test statistic, df=degrees of freedom, p_{perm}=Monte-Carlo permutation p-value, CI_{perm}=95% Monte-Carlo permutation confidence interval). Significant differences with Bonferroni-corrected p<0.0125 (correcting for 4 tests) are marked by *.

To investigate the mechanisms behind layer-specific thinning and thickening, we examined a healthy adult (male, age=52 years) with congenital arm loss at the right side. As expected, the hand area contralateral to the missing arm (identified via mental imagery of finger movements[21]) was thinnest (hand contralateral: 1.82 mm; hand ipsilateral: 1.88 mm; face contralateral: 1.96 mm; face ipsilateral: 1.93 mm). Critically, layer-specific cortical thickness extraction reveals a thinner middle compartment for the hand area contralateral compared to ipsilateral to the missing limb (hand contralateral: outer=0.38 mm, middle=0.83 mm, inner=0.67 mm; hand ipsilateral: outer=0.47 mm, middle=0.72 mm, inner=0.63 mm). Layer IV of SI is therefore thinner in a case with congenital arm loss in the hand area contralateral compared to ipsilateral to the missing limb, indicating that plasticity-based mechanisms influence thickness of SI layer IV. Note that layer-specific thickness values of the one-hander are in a plausible data range (taking the range of two-handed participants for the hand area as reference: outer=0.38-0.58 mm, middle=0.53-0.83 mm, inner=0.60-1.17 mm).

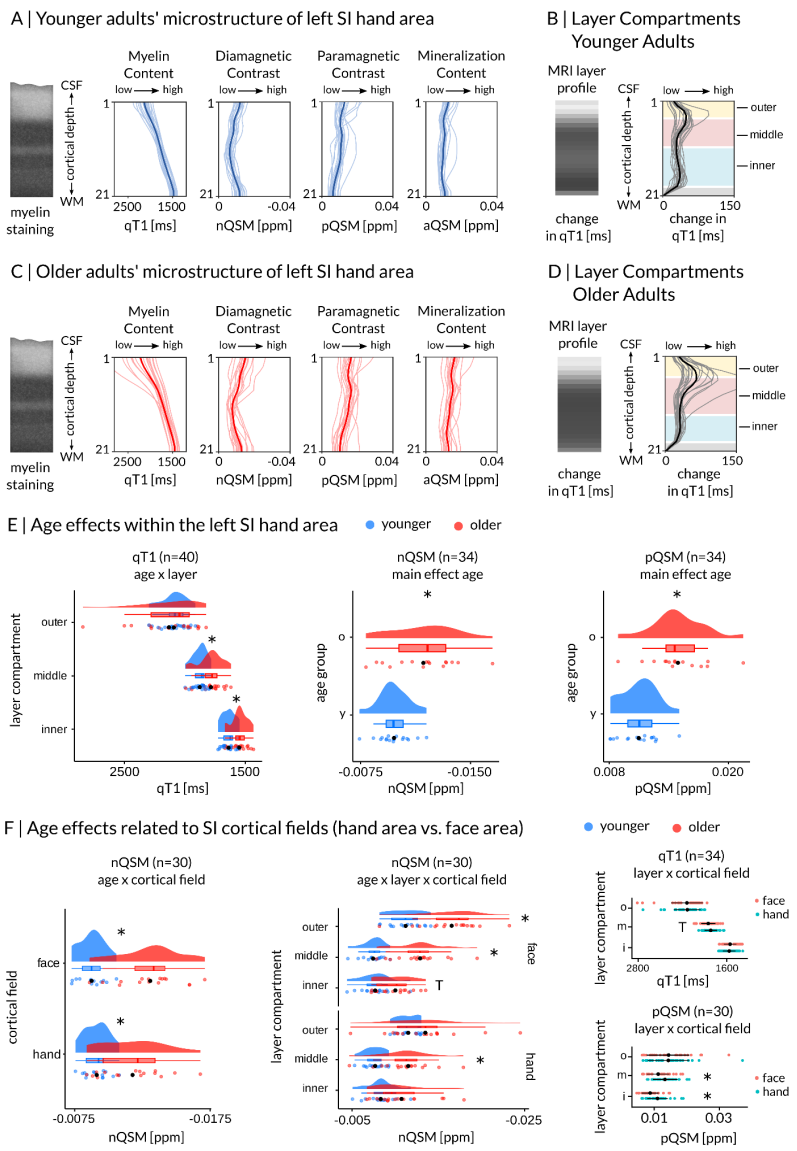

Figure 2. Aging Structural Layer Architecture in SI (A) Younger adults' microstructure described by qT1-based myelin (n=20), nQSM-based diamagnetic contrast (indicative of calcium content/metabolism; n=18), pQSM-based paramagnetic contrast (indicative of iron content; n=18), aQSM-based mineralization (n=18) sampled between the CSF/GM border and the GM/WM border (group mean plotted in bold). Low qT1 and nQSM indicate high myelin content and high diamagnetic contrast, respectively. Myelin staining was remodeled according to Dinse et al.[16]. **(B)** Layer compartments of younger adults (*cream*, outer layer; *light pink*, middle layer; *light blue*, inner layer) were calculated based on mean local rate of change in intracortical qT1[14]. The middle layer compartment (*light pink*) is assumed to reflect the heavy-myelinated Baillarger band running through anatomical layer IV. MRI layer profiles visualise the local rate of change in intracortical qT1 as shades of *grey*. **(C)** Older adults' microstructure described by qT1-based myelin (n=20), nQSM-based diamagnetic contrast (n=16), pQSM-based paramagnetic contrast (n=16), aQSM-based mineralization (n=18) sampled between the CSF/GM border and the GM/WM border (group mean plotted in bold). **(D)** Layer compartments of older adults calculated based on the mean local rate of change in intracortical qT1 (*black line*). **(E)** Age effects on qT1, nQSM and pQSM in the SI hand area (permutation mixed-effects ANOVAs), individual data shown as colored dots: younger adults [y] in blue, older adults [o] in red; group means shown as black dots. Box plots are drawn within the interquartile range (box), medians are shown as vertical lines, whiskers connect the minimum and the maximum with the lower and the upper quartiles. Significant differences at Bonferroni-corrected significance level of $p<0.0045$ are marked by a *. **(F)** Age effects on SI cortical fields, i.e., hand area vs. face area (permutation mixed-effects ANOVAs on residual qT1, nQSM and pQSM after regressing out the effect of map size). Significant differences at Bonferroni-corrected significance level of $p<0.002$ are marked by a *. Trends above Bonferroni-corrected threshold are marked by a T.

More pronounced sensory input signal in older adults

The above-reported results reject the 'preserved layer hypothesis' and point towards the 'altered input channel hypothesis', according to which older adults show specific alterations in the input layer IV. To follow this up, we investigated in a second sample (n=11 younger adults, n=10 older adults, layer-specific functional study) if the thicker input layer IV is associated with increased input signals to layer IV in older adults. We extracted stimulation-induced %signal change of finger representations (see **Fig. 3** for topographic arrangement, and **Fig.3-supplemental figure 2** for %signal change) in contralateral SI for each individual at each modeled cortical depth. As a non-sensory control condition, we also extracted mean signal fluctuations during rest from the same areas. In both younger and older adults, we observed an antagonistic center-surround relationship between signals and cortical depth. That is, signals peaked at the input layer IV but were minimal in neighboring depths. Given we only observed this relationship during sensory stimulation but not during rest, and the peak occurred at the expected layer compartment encompassing layer IV (defined based on independent structural data), the signal peak is a marker to measure input signals to layer IV in SI[22,23] (see **Fig. 3D** versus **3E**). Critically, older adults compared to younger adults present with a more pronounced sensory input peak and a more pronounced sensory input signal decay surrounding the input peak (see **Fig. 3F,G,H,I**, for detailed statistics **Fig. 3-supplemental table 1**). This provides additional evidence to confirm the 'altered input channel hypothesis'.

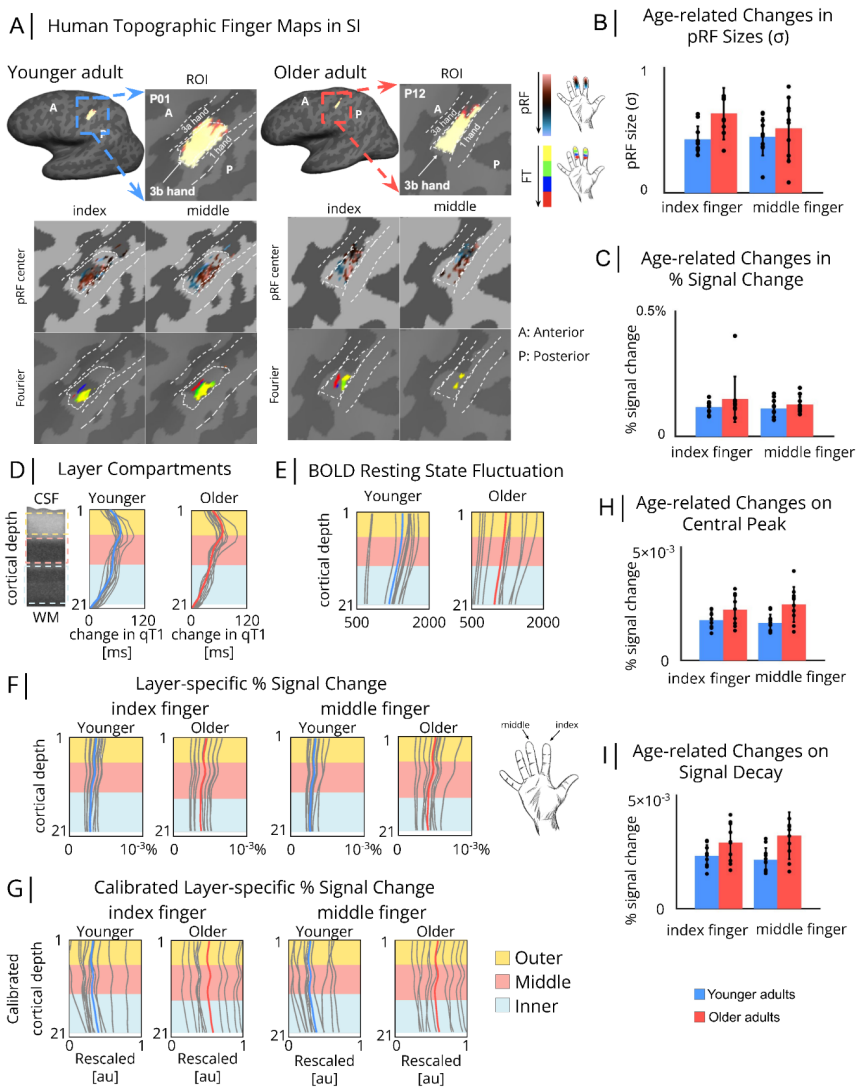

Figure 3. Layer-specific Functional Architecture of Human SI (A) Individual topographic maps of the index finger and the middle finger in younger adults and older adults, shown for one younger and one older exemplary participant (randomly chosen, younger: P01 and older: P12), see **Fig. 4-supplemental figure 1** for all individual data. Shown are topographic maps extracted using population receptive field (pRF) modeling (*first rows in each panel*) and Fourier-based mapping (*second rows in each panel*). ROI = Region-of-interest (hand area of contralateral area 3b). **(B)** Averaged pRF sizes (σ) estimates of index and middle finger (with arbitrary units (au), mean ± SD and individual data) for younger (*blue*) and older (*red*) adults. **(C)** Average % signal change of index and middle finger (mean ± SD and individual data) for younger (*blue*) and older (*red*) adults. **(D)** Layer compartments (*cream*: outer layer, *light pink*: middle layer, *light blue*: inner layer) for younger (n=11, *blue*) and older (n=10, *red*) adults defined based on the rate of change in qT1[14,16]. (**E**) Resting state signal fluctuation extracted at different cortical depths for younger (*blue*) and older (*red*) adults. **(F)** Layer-specific % signal change of index finger and middle finger representations in SI extracted at different cortical depths for younger (*blue*) and older (*red*) adults. **(G)** Layer-specific % signal change of index and middle finger representations using calibrated-BOLD (Blood Oxygen Level Dependent) extracted at different cortical depths for younger (*blue*) and older (*red*) adults. Values are scaled between 0 and 1. **(H)** Averaged central peak (mean±SD and individual data) of index and middle finger representations for younger (*blue*) and older (*red*) adults. **(I)** Averaged signal decay (mean±SD and individual data) of index and middle finger representations for younger (*blue*) and older (*red*) adults.

Altered microstructural layer composition in older adults and with congenital hand loss

To test our hypotheses, we also need to understand how the microstructural composition of specific SI layers changes with age. We extracted layer-specific qT1 values as a proxy for cortical myelin[16,24] and quantitative susceptibility maps (QSM) as proxies for cortical iron (positive values, pQSM) and calcium/metabolism (negative values, nQSM)[29,30,31], as well as overall mineralization (absolute values, aQSM)[28], using the hand area as ROI (localized by pRF mapping of the five fingertips of the right hand).

First, using univariate mixed-effects non-parametric permutation ANOVAs on qT1, nQSM, pQSM, and aQSM with between-subjects factor age (younger, older) and within-subjects factor layer compartment (inner, middle, outer), we confirm previously reported across-layer age effects[7,26,27,28]: (1) more negative nQSM values (higher calcium content/metabolism, older: -0.0118±0.0006 ppm; younger: -0.0098±0.0003 ppm), (2) higher pQSM values (higher iron content, older: 0.0149±0.007 ppm; younger: 0.0110±0.0004 ppm), and (3) higher aQSM values (higher mineralization content, older: 0.0138±0.0006 ppm; younger: 0.0103±0.0003 ppm) in older compared to younger adults (see **Fig. 2-supplemental table 1, Fig. 2-supplemental table 2**).

Critically, age effects on qT1 values are layer-specific, with lower qT1 values (reflecting higher myelin) in the inner and middle compartments in older compared to younger adults (older: inner=1547.6±14.8 ms, Mean±SE; middle=1783.2±21.9 ms; younger: inner=1636.3±12.3 ms; middle=1874.4±12.9 ms; see **Fig. 2E**, for exact results see **Fig. 2-supplemental table 1** and **Fig. 2-supplemental table 2**). Whereas the lower qT1 values in the middle compartment were expected due to the above reported greater input channel in older adults, the lower qT1 values in the deep compartment were not expected based on the above described cortical thinning of deep layers in older adults (for control analyses using a different compartmentalization scheme see **Fig. 2-supplemental table 3, Fig. 2-supplemental table 4**).

Controlling for effects of cortical atrophy, there is no significant difference in hand mask (full fingertip map) size (qT1 (n=40): $t(33.7)=-0.48$, $p=0.632$; nQSM (n=34): $t(31.8)=0.67$, $p=0.510$; pQSM (n=34): $t(30.1)=-0.39$, $p=0.696$; aQSM (n=34): $t(29.4)=0.02$, $p=0.981$) between younger (qT1: 1249±90; nQSM: 512±53; pQSM: 717±62; aQSM: 1271±98 vertices, Mean±SE) and older adults (qT1: 1325±130; nQSM: 462±53; pQSM: 756±75; aQSM: 1268±124 vertices) that could explain this effect.

qT1 values extracted from the deep compartment in the participant with congenital arm loss appear similar for the SI hand area contralateral and ipsilateral to the missing arm (localized by imagery of motor movements or actual motor movements, respectively), whereas the superficial compartment presents with higher qT1 values in the hand area contralateral to the missing arm (see **Table 2** for absolute values**, Table 2-supplemental figure 1** for microstructural profiles and layer compartmentalization scheme in reference to younger and older adults**, Table 2-supplemental figure 2** for microstructural profiles of map size adjusted ROIs). Myelin degeneration (as indicated by higher qT1 values) due to reduced sensory input may therefore affect superficial SI layers, while cortical aging is associated with lower qT1 values in deep SI layers. To clarify the role of age-related alterations in deep layers more precisely, additional analyses were conducted in older adults (see below).

	qT1	nQSM	pQSM	qT1	nQSM	pQSM
	contralateral to missing limb			ipsilateral to missing limb		
hand outer	2107.4	-0.017	0.015	2081.7	-0.012	0.016
hand middle	1678.5	-0.013	0.021	1705.3	-0.007	0.019
hand inner	1499.5	-0.011	0.022	1508.2	-0.009	0.019
face outer	2142.4	-0.018	0.021	2140.1	-0.019	0.020
face middle	1794.3	-0.020	0.016	1750.3	-0.018	0.019
face inner	1559.9	-0.013	0.015	1527.2	-0.011	0.015

Table 2. **Microstructural layer composition of SI hand and face areas of a participant with congenital arm loss.** Cortical fields (i.e. hand and face regions) were localized by motor movements or imagery of motor movements (for the missing limb condition). Given are layer-specific (outer, middle, inner) qT1 (in milliseconds), nQSM (in ppm), and pQSM (in ppm) values. Lower qT1 and nQSM values indicate higher substance concentration. For microstructure profiles plotted along the dimension of cortical depth see Table 2-supplemental figure 1 and Table 2-supplemental figure 2.

Altered functional response profile in older adults' SI

The 'altered modulation hypothesis' expects that deep layer degeneration (here evidenced via deep layer thinning) may reduce functional inhibition in older adults[3,12]. However, given deeper layers show reduced qT1 values (higher myelin content), also the reverse effect could appear. To target this, different functional metrics were extracted from the SI representations of the index finger and the middle finger contralateral to stimulation. Compared to the structural study design (where five fingers were touched at the fingertip only), we now restricted the experimental design to two fingers that were touched at multiple locations (also adding a 'double-finger stimulation' condition), allowing us to test these representations in greater detail (younger adults: n=11, older adults: n=10).

We first detected coarser spatial selectivity (i.e., larger population receptive field (pRF) size, sigma parameter (σ)) specifically of the index finger representation in older compared to younger adults (index finger: BF_{10}=11.97; middle finger: BF_{10}=1.07; see **Fig. 3B**, for detailed statistics see **Fig. 3-supplemental table 1**), confirming a previous observation[5]. We then used pRF modeling to quantify inhibitory and excitatory response properties for two single-finger conditions (index or middle finger) and one double-finger condition (index and middle finger) by comparing the difference between the average pRF size of the two single-finger conditions and the pRF size of the double-finger condition between age groups. We found no evidence for reduced inhibition in older adults (BF_{10}=0.876, see Fig.3-supplemental table 3 for detailed statistics). To use an established marker to quantify inhibition[31,32], we compared mean %signal change between single-finger and double-finger conditions, and again found no evidence for reduced inhibition in older adults (BF_{10}=1.424, see **Fig.3-supplemental table 3** for detailed statistics). Interestingly, this data suggests that deep layer thinning does not prompt decreased functional inhibition in older adults, but that more myelinated deep layers may trigger the reverse effect. Subsequent functional and structural analyses in aging mice were conducted to clarify this point (see section '*Functional overactivation and altered layer architecture in older mice*').

SI layer-specific structural topography in older adults and with congenital hand loss

Before reporting functional and structural analyses in aging mice to better clarify the 'altered modulation hypothesis', we tested the 'degraded border hypothesis'. This hypothesis assumes that the low-myelin borders that exist inferior to the thumb representation[13], and occasionally between single finger representations[14], in input layer IV of SI degenerate with age. This, too, could influence functional representations. To test this, we developed an

automatic border detection algorithm (**Fig. 2-supplemental figure 2A**). We found no age-related differences with respect to the existence or composition of layer IV low-myelin borders between younger and older adults (see **Fig. 2-supplemental figure 2B-D**). Statistical trends that indicate differences in iron and calcium content in the hand-face border between age groups (see **Fig. 2-supplemental figure 2C,D**) were not specific for the border area but were generally observed in SI. The same automatic border detection algorithm was applied to the participant with congenital arm loss, revealing that low-myelin borders similarly exist in both hemispheres, i.e., contralateral and ipsilateral to the missing arm (see **Fig. 4-supplemental figure 2**). Low-myelin borders therefore remain stable both with age and with congenital arm loss. This rejects the 'degraded border hypothesis', confirming a previous observation in human MI[7].

To investigate age-related changes in SI structural topography more comprehensively, we also tested whether there are age- and layer-specific structural changes that only affect certain topographic representations. We performed univariate mixed-effects non-parametric permutation ANOVAs with between-subjects factor age (younger, older) and within-subjects factors layer compartment (inner, middle, outer) and finger (thumb-little finger) on qT1, nQSM, pQSM and aQSM (see **Fig. 2-supplemental table 5, Fig. 2-supplemental table 6** for different compartmentalization scheme). Controlling for the effect of map size (i.e., regressing out the number of vertices), individual finger representations do not significantly differ in their microstructural composition (confirming a previous observation in younger adults[14]), and aging does not affect certain finger representations more than others. However, intracortical qT1 and pQSM values differ significantly between the hand and face representations in SI across age groups, specifically in the middle and inner layer compartments (indicating distinct cortical fields; see **Fig. 2F**, **Fig. 2-supplemental table 7** and **Fig. 2-supplemental table 8** for exact results). For nQSM, these effects are age-specific, showing more pronounced age differences in the face area compared to the hand area (see **Fig. 2F, Fig. 2-supplemental table 8**). These differences are characterized by significantly more negative nQSM values in the outer and middle compartments, and a trend for significantly more negative nQSM values in the inner compartment of the face area in older compared to younger adults. For the hand area, the age effect is restricted to the middle compartment (see **Fig. 2F**). Taken together, whereas low-myelin borders between the hand and face areas are stable with aging, the face area itself shows greater age-related changes than the hand area, confirming a previous observation in MI[7].

Functional overactivation and altered layer architecture in mice

While BOLD responses are difficult to relate to precise neural excitatory or inhibitory drive, and MR data are difficult to relate to precise histological changes, the use of animal models can help us to clarify mechanistic aspects related to the cytoarchitectural changes observed in deeper layers. We investigated single-neuron activity in younger (n=8, 4-5 months) and older (n=8, 14-20 months) mice and combined this with post mortem histological analysis across cortical layers. We examined the aging whisker barrel cortex in mice as an analogous sensory system that shares multiple topological features and aspects of cortical representation with the human hand and fingers[15].

To first examine sensory-driven activation in older compared to younger mice, a cranial window was implanted above the barrel cortex in transgenic mice expressing a genetically encoded calcium indicator (CGaMPf)[33] driven by a Thy1 promoter[34]. We examined sensory-evoked responses of excitatory neurons across the outer (layer II/III) and inner (layer V) cortical layers following airpuff stimulation to subsets of whiskers (see **Fig. 1C**). Changes in fluorescence (ΔF/F) of the calcium indicator were extracted and used as a proxy readout of neuronal activity (**Fig. 4A**). On the single-cell level, we observed heterogeneous responses across whisker stimulation conditions (all whiskers, two neighboring whiskers [W1+W2], and single whisker [W1] stimulation), with some neurons showing responses to all conditions and others showing modulation to specific stimulation conditions (**Fig. 4A**). We observed a shift in the distribution of sensory-evoked responses in older mice, with larger amplitude responses compared to younger mice (**Fig. 4B**), indicating an overactivation with aging. Comparing the average ΔF/F responses across all neurons within a field-of-view for younger and older mice, we found a significant effect of both age ($p<0.001$) and stimulation condition ($p=0.045$), with older mice showing larger sensory-evoked excitatory neuronal responses compared to younger mice (**Fig. 4B;** two-way mixed-effects ANOVA, constrained (type III) sum of squares; Tukey-Kramer correction).

Similar to the pRF modeling in humans that found a trend towards increased inhibitory interactions within individual vertices in SI with age, we found suppressive influences of the double whisker stimulation in comparison to the single whisker stimulation in spatially averaged activity maps (**Fig. 4C**). This was also observed on the single-cell level in the percentage of responsive neurons across age and cortical layers (**Fig. 4D**). Particularly in the outer cortical layers (layer II/III), younger mice show an increased proportion of individual neurons with additive responses (younger: 65%, older: 51%) while older mice show a higher proportion of neurons with reduced sensory-evoked responses (younger: 13%, older: 23%)

in the double whisker condition compared to the single whisker stimulation. Therefore, we found evidence for both sensory-evoked overactivation in older mice as well as increased functional inhibition of neighboring whiskers; mirroring and extending the results in humans.

Following this functional similarity, we examined cytoarchitectural changes across layers in the barrel cortex of younger and older mice (**Fig. 4E**). We found a trend towards a main effect of age driven by reduced overall cell density in older mice (p=0.062), no main effect of layer (p=0.292), and a trend towards an interaction between age and layer (p=0.100) in the overall cell density. To clarify the hypothesis if lower qT1 values in deep layers of older adults in humans drive increased functional inhibition (i.e., 'altered modulation hypothesis'), we conducted post-hoc comparisons in older mice, which revealed a significant decrease in cell density in older mice from the outer layers to inner layers (p=0.031; two-way mixed-effects ANOVA, constrained (type III) sum of squares; Tukey-Kramer correction; **Fig. 4F**). To assess changes specific to inhibitory drive, we examined the proportion of neurons expressing parvalbumin (PV+), which is a molecular marker of the largest class of inhibitory interneurons in the cortex[35]. We found a significant effect of age driven by increased PV+ density in older mice (p<0.001) and layer (p<0.001), but no interaction (p=0.141, two-way mixed-effects ANOVA, see **Fig. 4F** for details).

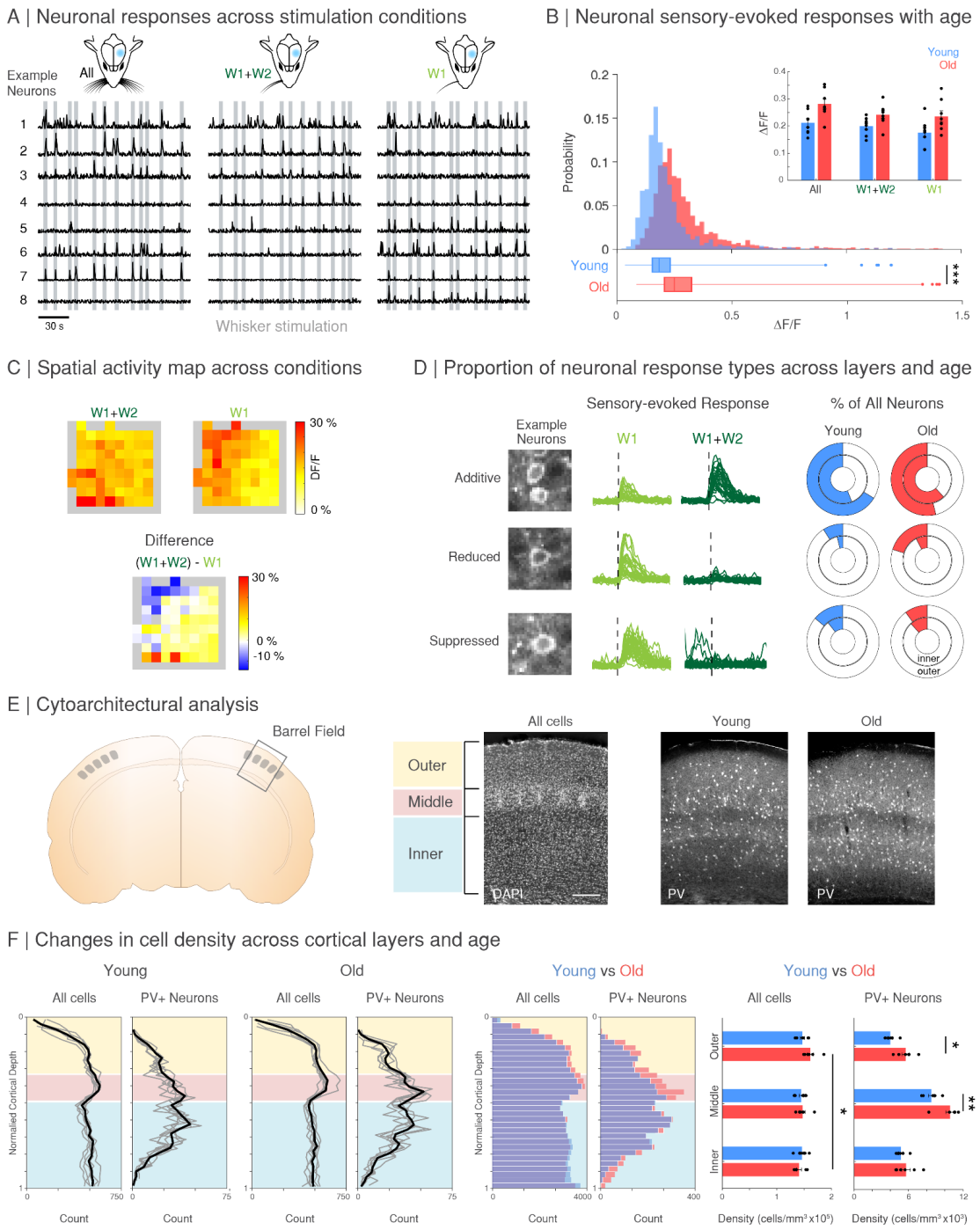

Figure 4. **Age-Related Functional and Structural Changes in Mouse Barrel Cortex (A)** Calcium activity from example neurons (1-8) for the three stimulation conditions, all whiskers (All), two neighboring whiskers (W1+W2), and single whisker (W1) stimulation **(B)** Histogram of the average sensory-evoked change in fluorescence (ΔF/F) for all neurons and population averages across young and old mice (n = 8 mice each). **(C)** Sensory-evoked ΔF/F for an example field-of-view, averaged across 50 x 50 pixel spatial bins during double whisker (left) and single whisker (right) stimulation and the difference of these two conditions (below). **(D)** Example neurons and sensory-evoked ΔF/F that show additive, reduced, or suppressed responses to single (W1) or double (W1+W2) whisker stimulation; percentage of neurons showing these response types in young (blue) and old (red) mice across outer (layer II/III) and inner (layer V) cortical layers. **(E)** Schematic of the mouse barrel field where images of 4′, 6-Diamidin-2-phenylindol (DAPI) staining of all cells and parvalbumin (PV) immunohistochemistry from the barrel cortex were collected across young and old mice. Scale bar 100μm. **(F)** Cortical depth was normalized from the brain's surface (0) to the white matter (1); cell counts are displayed as a binned sum along the cortical depth (gray lines, individual mice; black line, average across mice), and compared between young and old mice (n = 6 mice each). The density of all cells (DAPI) and PV expressing cells is shown across layers and age (right).

Relation between layer-specific changes and human sensorimotor impairments

Finally, we investigated whether interindividual variation in layer-specific microstructure and function is related to age-specific functional and behavioral decline in humans. We first confirm that older adults compared to younger adults show worse tactile performance (impaired detection, impaired 2-point discrimination, trend for impaired finger discrimination, for exact results see **Fig.5-supplemental table 1**), worse hand dexterity (impaired Grooved Pegboard Test, O'Conner Hand Dexterity Test, and Small Motor Test performance, for exact results see **Fig.5-supplemental table 2**) and worse sensorimotor integration at the hand (see **Fig.5-supplemental table 1**). Kendall's tau correlation coefficients were then calculated for older adults (see **Fig. 5**), which revealed the following insights: In older adults (1) lower qT1 values (higher myelin content) in the deep layer compartment are associated with higher network centrality, whereas lower qT1 values (lower myelin content) in the superficial layer compartment are associated with lower network centrality, (2) lower qT1 values (higher myelin content) in middle and deep layer compartments of the index finger representation are associated with worse tactile detection and 2-point discrimination performance of the index finger, and (3) increased input signal central peaks for index finger and double finger representations correlate with better hand dexterity. These descriptive results can be taken into consideration when discussing structural and functional layer-specific changes in the cortex in a broader context.

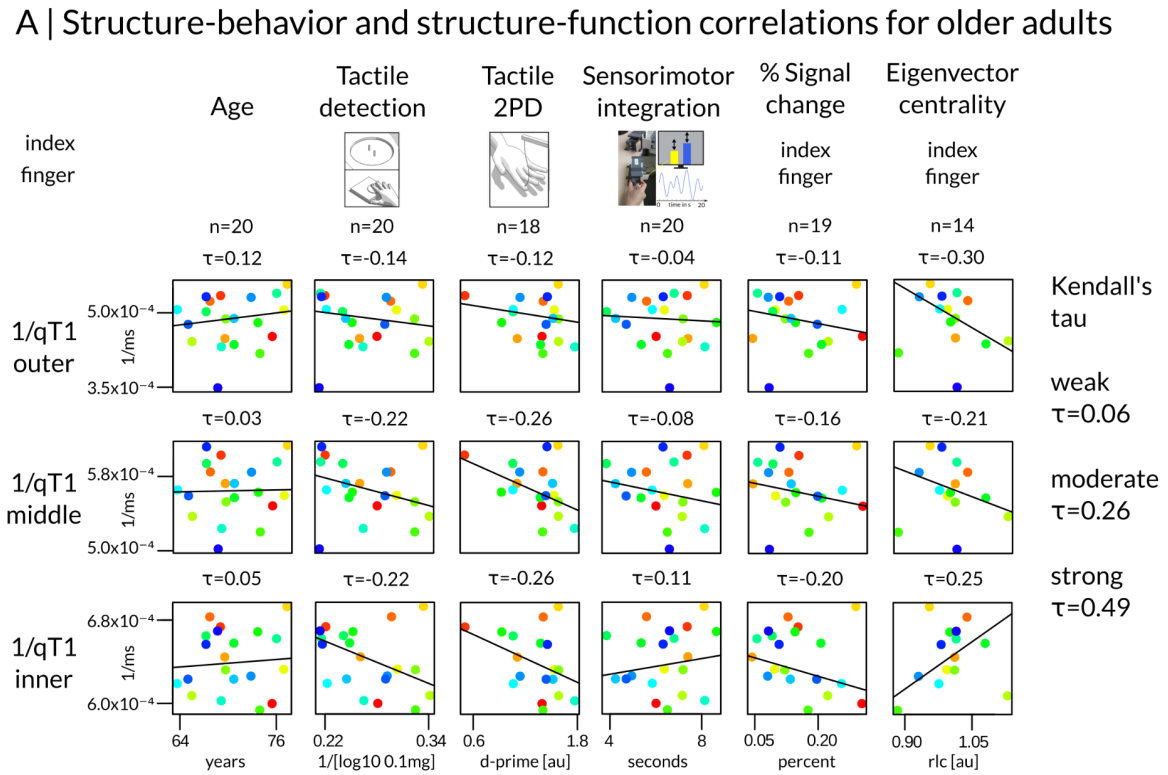

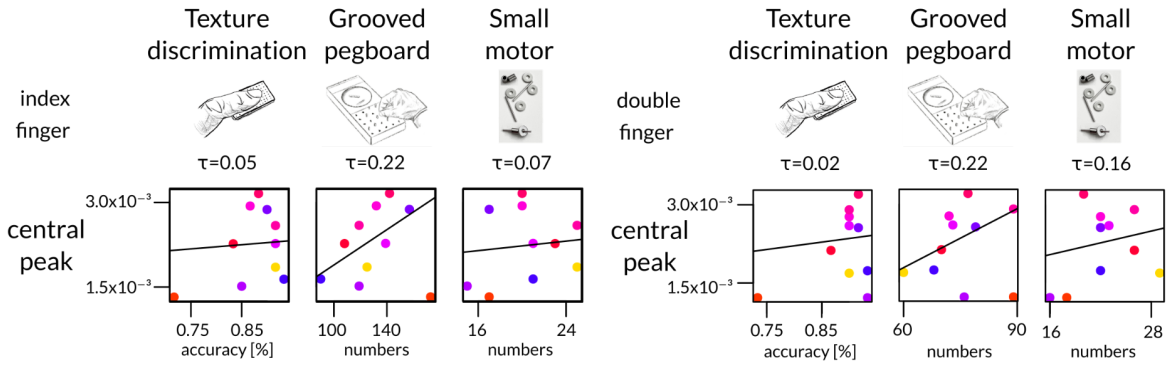

Figure 5. Relation between layer-specific changes and sensorimotor impairments in older adults. (A) Structure-function and structure-behavior correlations shown for the index finger representation. Regression lines were generated based on robust Theil-Sen regression estimates[36,37]. Correlation coefficients are given as Kendall's tau. Cut-offs for the interpretation of Kendall's tau were approximated by applying the formula tau=2/π arcsin(r) to cut-offs for the Pearson correlation coefficient (r)[38,39]. To ensure that higher values indicate better performance or more myelin, tactile detection and qT1 values (given in milliseconds) were reversed. Network centrality is given as rectified linear unit correlation in arbitrary units (au), tactile 2-point discrimination performance (tactile 2PD) is given as dprime in arbitrary units (au). **(B)** Function-behavior correlations shown for index finger and index-middle finger pair. Correlation coefficients are given as Kendall's tau.

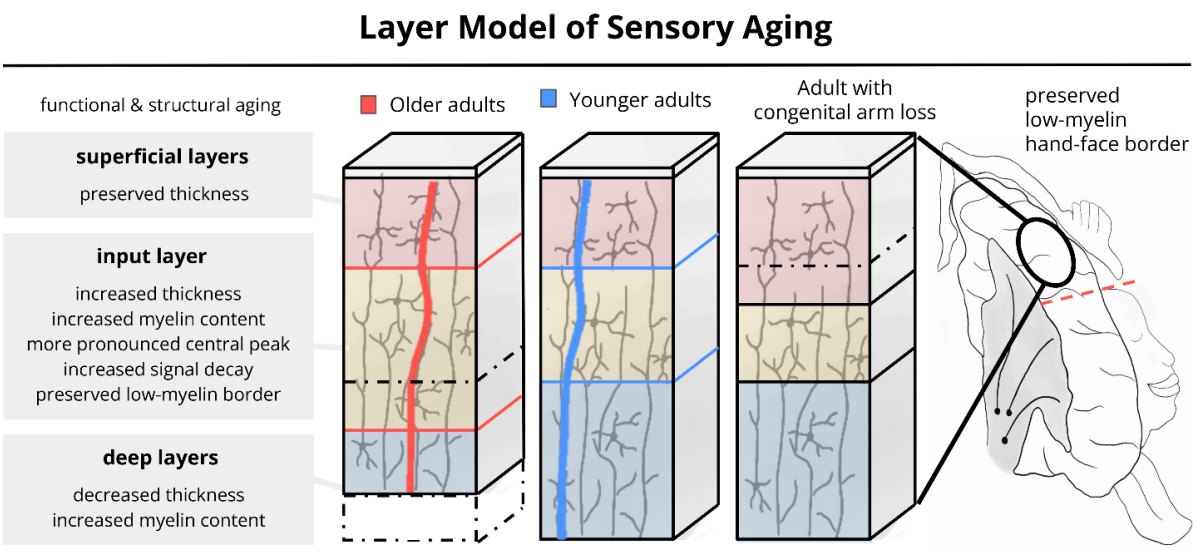

Figure 6. Layer Model of Sensory Aging. The layer model of sensory aging suggests that cortical aging, as one example of cortical dysfunction, has a unique layer-specific profile. Critical characteristics are a widened input channel with aging (but a reduced input channel with sensory deprivation), a layer-specific profile of cortical thinning driven by deeper layer degeneration, and altered modulatory influences from deep layers on functional representations.

Discussion

We studied the layer-specific structural and functional architecture of SI using *in-vivo* ultra-high field 7T-MRI data of healthy younger and older adults and an adult with congenital arm loss. We also investigated SI whisker representations in younger and older mice using *in-vivo* 2PCI in combination with histology to derive more information on potential underlying neuronal mechanisms. Altogether, our data reject the idea that the principle layer architecture of the sensory cortex is preserved with aging. Rather, cortical thinning is driven by deep layers, and the middle compartment, likely encompassing layer IV, appears thicker in older adults compared to younger adults. Whereas MI shows vulnerability in the output layer V and superficial layers in aging[7], in SI, superficial layers seem preserved and age-related changes appear in input and deep modulatory layers. These novel insights suggest that layer-specific degeneration is dependent on the specific microstructural architecture of the cortex, and needs to be described separately for different cortical areas.

We here introduce a novel model of layer-specific sensory aging (summarized in **Fig. 6**). Critical characteristics are a widened sensory input channel, layer-specific cortical thinning, and altered modulatory influences from deep layers on functional representations. This prompts novel research on layer-specific alterations in the cortex in health and disease.

Older adults present with a thicker and more myelinated input layer that exhibits a more pronounced sensory input signal peak. This confirms the 'altered input channel hypothesis' specifying a wider input channel in older adults' SI. When investigating an adult with unilateral congenital arm loss, we further learned that when lifelong sensory input to a body part is reduced, layer IV contralateral but not ipsilateral to the missing arm is thinner. An experience-driven mechanism influencing layer IV thinning and thickening is therefore likely[8,40]. The more pronounced layer IV in older age may reflect use-dependent plasticity over the individual lifespan, allowing individuals to compensate for peripheral signal loss, indicated here by worse tactile detection, by shifting short-range connections towards inhibition to sharpen sensory signals and/or stabilize established functional networks[41].

Critically, we show that age-related cortical thinning in humans is layer-specific. The usual across-layer estimate of cortical thickness, that is often used to describe the human cortex in health and disease, seems not as informative as previously assumed, in particular given the middle compartment of SI is thicker in older adults. In neurodegenerative diseases, such as Alzheimer's Disease (AD), cortical thinning is related to cell loss[42] and sensitive to early detection of neuropathology[43]. In the present work, older mice show reduced cell density in

deep layers compared to superficial layers. One may speculate that cortical thinning of deep layers in humans is linked to overall cell loss in these layers. This motivates extended research using layer-specific cortical thickness investigations to disentangle healthy from pathological aging.

We also detected more myelinated deeper layers in older adults, whereas functional inhibition is preserved or even increased in older adults. Both measures may be connected given deeper layers in SI are involved in subcortical signal integration, signal modulation and inhibition[44,45]. Whereas the BOLD effect has limitations with respect to its interpretation as excitatory or inhibitory[44], we replicated the inhibition effect in older mice using single-neuron activity. In addition, we found higher PV+ cell density in older mice, where previous work in mice has shown that a large fraction of myelin in cortical layers II/III and cortical layer IV ensheaths axons of GABAergic interneurons, particularly of PV+ basket cells in SI[45]. In humans, PV+ interneurons contribute substantially to the total myelin content in the cerebral cortex[46,47]. One way to explain the apparently puzzling result of higher myelinated but thinner deep layers in older adults as well as no reduction in functional inhibition is to assume that the decreased qT1 signal reflects changes in myelination linked to an increase in PV+ cell density. Thinner deep layers, on the other hand, may reflect reduced overall cell density[47,48,49,50]. This may provide a mechanistic explanation for the preserved or even increased functional inhibitory responses in SI in humans and mice.

It is worth noting that in older mice compared to younger mice, PV+ cell density is also increased in superficial layers (whereas in humans, increased myelination was restricted to middle and deep layers). If our interpretation of the ‘altered modulation hypothesis’ is correct, this suggests that cortical layer inhibition is differently affected in humans and mice with aging. An alternative explanation for the qT1 effect specifically in deep layers is that myelin sheaths are degrading (i.e., becoming less compact) due to sheath splitting and the formation of myelin balloons, which is accompanied by the production of redundant myelin and an increase in oligodendrocytes in older age[52]. In this view, the preserved or increased functional inhibition with age would be mediated by a more myelinated layer IV in both humans and mice. Future studies focusing on cytoarchitectural changes in relation to changing myelin patterns and sensory processing will solve this critical question.

The present findings have multiple clinical implications. Previous studies described dysfunction of cortical circuits, cortical thinning and/or a disturbed excitation/inhibition balance in a variety of psychiatric and neurological disorders, including schizophrenia, AD, Parkinson's Disease, Epilepsy, Multiple Sclerosis (MS) or Amyotrophic Lateral Sclerosis

(ALS)[52,53,54,55,56,57,58,59]. Our study reveals that in particular the combined investigation of layer-specific thickness, microstructural layer compositions and layer-specific functional readouts uncovers key aspects of cortex organization. In MS, for example, where neuroinflammation causes myelin damage and/or myelin loss in specific cortical layers[60], post-mortem investigations in humans showed a decrease in PV+ interneurons[61], which is in line with findings in mice[62]. This suggests an interaction between layer-specific myelination and excitation/inhibition modulation that could be investigated in-vivo with the methodology introduced here. Losing myelin progressively can result in epilepsy-like brain activity, as inhibition of slow brain waves decreases[63], and epileptogenic hyperexcitability and lesions often present layer-specific[64,65,66]. A multimodal layer-specific investigation could help lesion detection and uncover underlying mechanisms. The methods introduced here may allow the investigation of high-precision cortex pathology, for example in AD and ALS, allowing to tailor interventions and therapies to the specific patient.

Methods

Human participants

The present investigation combines data from two separate studies (layer-specific structural study, layer-specific functional study, see details below), in which two groups of younger and two groups of older adults underwent 7T-MRI and behavioral measurements. In the layer-specific structural study, 46 healthy volunteers underwent structural 7T MRI, functional localizers of individual fingers, as well as behavioral tests of tactile finger performance. Due to severe motion artifacts in the imaging data, 6 participants were excluded from the study, leaving a total of 40 participants for analyses (20 younger adults (10 females, 21-29 years, Mean±SD: 25.1±2.7 years) and 20 older adults (10 females, 63-77 years, Mean±SD: 70.5±4.0 years). In the layer-specific functional study, a total of 21 healthy, right-handed younger adults and 17 healthy older adults underwent behavioral measurements, of which, 14 younger adults and 13 older adults underwent 7T fMRI with a detailed investigation of the index and middle finger only. Due to severe head motion during scanning, 3 younger adults and 3 older adults had to be excluded, leaving 11 younger adults (5 female, 25-35 years, Mean±SD: 28.18±3.06 years) and 10 older adults for analyses (3 female, 60-80 years, Mean±SD: 68.40±6.20 years).

According to the Edinburgh handedness questionnaire[67], in the layer-specific structural study, all participants were right-handed (laterality index ranging from +40 to +100; Mean±SD: 83.93±19.56). Chronic illness, central acting medications and MRI contraindications (e.g., active implants, non-removable metallic objects, tattoos, claustrophobia, tinnitus, consumption of alcohol and drugs, and pregnancy) were a priori exclusion criteria for both studies. A study-specific health screening revealed no anomalies of sensory perception (e.g., numbness, tingling sensations, hypersensitivity, hyperalgesia) and motor movement (e.g., loss of motor control, restricted finger movement) in distal extremities. Given enhanced cortical hand representations and superior tactile perception in string and piano players[58,59,60], no professional musicians were enrolled in either study. We note that 2/20 older participants of the layer-specific structural study underwent successful carpal tunnel surgery on either the right hand only or on both hands. However, their tactile performance was absent of clinical signs (no outliers detected in the data), leading us to keep the data in the analysis. Besides, participants reported no other medical conditions. Finally, none of the participants showed signs of cognitive impairments as indicated by the 'Montreal Cognitive Assessment' (MoCA; score ≥ 26 used as criterion; younger adults Mean±SD: 29.0±1.1; older adults Mean±SD: 27.8±2.2)[71], except for one older adult with a MoCA score of 21. Because this participant performed equally well in the behavioral tasks

compared with all other older adults, we kept the data in the analysis. In addition, we collected data of one healthy adult with congenital arm loss (male, age: 52 years, affected side: right, level of deficiency: below shoulder, cosmetic prosthesis worn>8 hours per day, prosthesis never involved in daily life routines).

Younger and older adults from both studies were recruited from the database of the German Center for Neurodegenerative Diseases (DZNE) Magdeburg, Germany. The participant with congenital arm loss was recruited from the database of the Central Institute of Mental Health (CIMH) Mannheim, Germany. All participants gave written informed consent and were paid. The study was approved by the Ethics committee of the Otto-von-Guericke University Magdeburg. Data of younger and older adults were partly published in previous studies[5,7,14].

General procedure

Younger and older adults who participated in the layer-specific structural study attended four sessions: (1) structural 7T-MRI, (2) behavioral testing of tactile 2-point discrimination, tactile detection, sensorimotor integration, (3) behavioral testing of finger discrimination, (4) functional 7T-MRI (see **Fig. 1** for experimental design and analysis pipeline). In addition, all participants (including the one-handed adult) attended one 7T-fMRI session to collect functional localizers of large-scale body parts in MI and area 3b of SI (i.e., hand, face, foot representations)[7,14]. Younger and older adults who participated in the layer-specific functional study attended four sessions: (1) behavioral measurement (including tactile detection, hand dexterity and sensorimotor tasks), (2) structural 3T-MRI, (3) combined structural and functional 7T-MRI, and (4) functional 7T-MRI (see **Fig. 1** for experimental design and analysis pipeline).

Human MR scanning

Human 7T MRI

We used a whole-body 7-Tesla MAGNETOM scanner (Siemens Healthcare, Erlangen, Germany) equipped with a 32 Channel Nova Medical head coil to acquire MP2RAGE[72] images with whole brain coverage in both the layer-specific structural study and the layer-specific functional study (0.7 mm isotropic resolution, 240 sagittal slices, FoV read=224 mm, TR=4800 ms, TE=2.01 ms, inversion time TI1/TI2=900/2750 ms, flip angle (α)=5°/3°, bandwidth=250 Hz/Px, GRAPPA 2). In addition, for the layer-specific structural study, we acquired MP2RAGE images with part brain coverage (targeting the sensorimotor cortex; 0.5 mm isotropic resolution, 208 transversal slices, FoV read=224 mm, TR=4800 ms, TE=2.62

ms, inversion time TI1/TI2=900/2750 ms, flip angle (α)=5°/3°, bandwidth=250 Hz/Px, GRAPPA 2, phase oversampling=0%, slice oversampling=7.7%), and susceptibility-weighted images with part brain coverage (targeting the sensorimotor cortex) using a 3D gradient-echo pulse sequence[73] (0.5 mm isotropic resolution, 208 transversal slices, FoV read=192 mm, TR=22 ms, TE=9.00 ms, flip angle =10°, bandwidth=160 Hz/Px, GRAPPA 2, phase oversampling=0%, slice oversampling=7.7%). Structural scanning lasted in total approximately 60 minutes for the layer-specific structural study and about 20 minutes for the layer-specific functional study (because no 0.5 mm resolution images were acquired).

To acquire fMRI data, we first performed shimming and acquired two EPIs with opposite phase-encoding (PE) polarity before the functional time-series were collected using EPI gradient-echo pulse sequences (layer-specific structural study: 1 mm isotropic resolution, FoV read: 192 mm, TR=2000 ms, TE=22 ms, GRAPPA 4, interleaved acquisition, 36 slices; layer-specific functional study: 0.9 mm isotropic resolution, 30 slices, interleaved acquisition, FoV read=216 mm, TR=2000 ms, TE=22 ms, GRAPPA 4). The same sequence was used for all functional tasks (see below).

Human 3T MRI

3T MRI data were acquired at the Philips 3T Achieva dStream MRI scanner, where a standard structural 3D MPRAGE was acquired with the following parameters: resolution: 1.0 mm, 192 slices, FoV read=192 mm×256 mm, slab thickness=256 mm, TI=650 ms, echo spacing=6.6 ms, TE=4.73 ms, flip angle=8°, bandwidth=191 Hz/Px.

Human fMRI tasks

In the layer-specific structural study, we used a previously established tactile stimulation paradigm[5,14]. During the tactile task, five independently-controlled MR-compatible modules were used to stimulate the five fingertips of the right hand (each with 8 piezoelectric-controlled pins arranged in a 2×4 matrix, covering 3.5×8.5 mm^2 of skin; Quaerosys, http://www.quaerosys.com, see **Fig. 1**)[64,65,66]. Individually-adjusted vibrotactile stimulation was applied at a frequency of 16 Hz[77] using 16 pin combinations per second[64,65,66], raising 2 pins at a time. First, a phase-encoded protocol was applied (2 runs of 20 cycles; each fingertip stimulated 20 times for 5.12 seconds) in forward (thumb to little finger, 50% forward-run first) and reverse order (little finger to thumb, 50% reverse-run first). One run took 8 minutes and 32 seconds (256 scans, TR of 2 seconds). Participants counted randomly occurring stimulation pauses and had to report them after each run. A blocked-design protocol was used to stimulate the fingers in a pseudo-random way (2 runs;

6 conditions: stimulation to thumb, index, middle, ring, little finger and no stimulation), using the same instructions and stimuli as described for the phase-encoded protocol. One run took 6 minutes and 56 seconds (each fingertip was stimulated 10 times for 2 seconds followed by a 22 seconds resting phase; inter-stimulus intervals of 2 seconds in 70% of trials or 6 seconds in 30% of trials were counterbalanced between fingers; 208 scans). Finally, we acquired resting-state data in a 5-minute scan while participants looked at a fixation cross and were asked to think about nothing in particular. Total scan time was approximately 40 minutes.

A subsample of participants of the layer-specific structural study (n=34) underwent the same motor paradigm as described in Northall et al.[7]. In short, we used a blocked-design paradigm where participants carried out motor movements of the left and the right hand, the left and the right foot and the tongue, which we used to locate the face-hand area in BA 3b. Participants were trained outside the MR scanner and wore fingerless braces to stabilize the hand while carrying out precise movements. Movements were carried out for 12 seconds followed by a 15 seconds rest period. Movements were repeated four times each resulting in 20 trials in total. For the one-handed adults we applied a modified version of the original motor paradigm using mental imagery of finger movements for the missing limb.

For the layer-specific functional study, the same modules as described above were used to stimulate the distal phalanges and intermediate phalanges of the index and middle finger of the right hand. One module was attached to each phalanx using a custom-build, metal-free applicator that fitted individual finger sizes. The vibrotactile stimulation was applied at a frequency of 16 Hz, and the stimulation intensity of each finger was adjusted to two times of the individual tactile detection thresholds. To minimize adaptation-related differences in map activity between individuals, three randomly chosen pins were raised once at a time, yielding 16 pin combinations per second. Participants underwent two blocked-design runs and twelve phase-encoded runs. For each run, participants were asked to look at a centrally presented fixation cross. The blocked-design run comprised three conditions, including stimulation to index, middle finger and a rest condition with no stimulation. Each finger was stimulated for 8 seconds in a pseudo-random sequence, where one finger was stimulated maximally two times in a row. In 70% of the trials, there was a 4 seconds pause between two subsequent stimulations, in 30% of the trials, there was a 8 seconds pause between two subsequent stimulations. This was counterbalanced across fingers. Each finger was stimulated 20 times. One run comprised 264 scans, and lasted for 8 minutes and 48 seconds. The blocked-design run was repeated twice, lasting around 20 minutes in total. The phase-encoded runs included three different conditions: (1) stimulation of both the index

finger and the middle finger, (2) stimulation of the index finger (3) stimulation of the middle finger. Each condition comprised four runs, each consisting of eight stimulation cycles and two rest conditions of 32 seconds (one before and one after stimulation). Each stimulation cycle lasted 32 seconds, and stimulation was applied to each section of the phalanx four times for 8 seconds. Half of the stimulation runs of each condition were delivered in a forward order (top→down) and the other half in a reverse order (down→top) (see **Fig. 1**). Half of the participants of each age group started with the forward-run, the other half started with the reversed-run. One run comprised 160 scans (128 scans for stimulation and 32 scans for rest), lasting 320 seconds for a TR of 2 seconds. Participants were instructed to covertly count short randomly distributed interrupts embedded in the tactile stimulation (duration 180 ms, slightly longer than in Schweisfurth et al.[74, 76,75], the same as in Liu et al.[5]). There were the same number of gaps in each run (32 gaps in total). All phase-encoded runs took around 60 minutes.

Human physiological data recording

A pulse oximeter (NONIN Pulse Oxymeter 8600-FO) clipped to the participant's left index finger (no module attached) captured the pulse, and a breathing belt captured respiration during fMRI. Signals were digitally recorded with a sampling frequency of 200 Hz using an in-house developed setup (National Instruments USB 6008 module with pressure sensor Honeywell 40PC001B1A).

Human MRI analyses

3T structural data surface reconstruction

Csurf (http://www.cogsci.ucsd.edu/~sereno/.tmp/dist/csurf) recon-all (implanted from Freesurfer (v7.3.0) (http://surfer.nmr.mgh.harvard.edu/) was used for brain segmentation and cortical surface reconstruction using the T1-weighted 3D MPRAGE image. As a fully automated processing pipeline, recon-all performs steps including intensity correction, transformation to Talairach space, normalization, skull-stripping, subcortical and white matter segmentation, surface tessellation, surface refinement, surface inflation, sulcus-based nonlinear morphing to a cross-subject spherical coordinate system, and cortical parcellation[78,79]. Skull stripping, segmentation and surface inflation quality were checked for each participant.

7T structural data preprocessing

In the layer-specific structural study, quantitative susceptibility images (QSM) were reconstructed from 3D GRE magnitude and phase images using the Bayesian multi-scale dipole inversion (MSDI) algorithm[80] as implemented in QSMbox (version 2.0, freely available for download: https://gitlab.com/acostaj/QSMbox). No normalization was applied to QSM values, because aging effects are assumed to be similar for normalized and non-normalized 7T MRI data[28].

Two independent raters evaluated structural data quality of QSM and qT1 images (with the effect of excluding data of n=6 participants with severe motion artifacts). Only data showing no artifacts or mild truncation artifacts (not affecting SI) were processed. We used the same processing pipeline as described previously[14], employing CBS Tools (v3.0.8) as a plugin for MIPAV (v7.3.0). In short, we co-registered qT1 slab images to upsampled qT1 whole brain images (combining linear and non-linear registration using ANTs version 1.9.x-Linux, embedded in CBS Tools)[81] in one single step (nearest neighbor interpolation). To register QSM slab images to qT1 images, a combination of rigid and affine automated registration was applied using ITK-SNAP (v3.8.0). Registered qT1 slab and upsampled qT1 whole brain images were fused. Resulting images were skull stripped and dura removed. Dura estimates were manually refined where required to ensure complete removal of non-brain matter from the region of interest. We used the TOADS algorithm[82] to segment the cortex from the rest of the brain before we applied the CRUISE algorithm[83] to estimate tissue boundaries using the level set framework[84]. Cortex estimates were thresholded between the maximum of the inner and outer level set images (-2.8 and -0.2, respectively). Afterwards, the cortex was divided into 21 cortical depths using the validated equivolume model[85,86]. Intra-cortical qT1 values (used as proxy for myelin)[24] and QSM values (used as proxies for iron [positive values][26,29,80]; calcium/diamagnetic contrast [negative values][30,77,78,79,80]; and mineralization [absolute values][28]) were sampled along the extracted cortical depths in reference to individual cortical folding patterns. Individual cortical surfaces were estimated based on level set images of the middle cortical depth. Layer-specific quantitative values of the non-merged high-resolution qT1 and QSM slab images were mapped onto the inflated cortical surfaces (method of closest point)[91].

In the layer-specific functional study, first, structural data quality was evaluated for each participant. Data showing severe artifacts (i.e., n=2 participants) were excluded. Only data showing mild truncation artifacts (not affecting SI) or no artifacts at all were used. All structural MP2RAGE images were sent to a pipeline including background noise cleaning,

inhomogeneity correction, brain segmentation, cortical reconstruction and layer surface mapping. Background noise in all T1-weighted images was removed using the code of José P. Marques (https://github.com/JosePMarques/MP2RAGE-related-scripts) and the method described in O'Brien et al.[92]. Skull stripping was performed on T1-weighted images using Freesurfer (v7.3.0) mri_synthstrip routine[93]. Based on the white matter (WM), gray matter (GM), and cerebrospinal fluid (CSF) segmentations, a brainmask was created and applied to the qT1 images for consistency. Inhomogeneity correction was done for both qT1 and T1-weighted images using the segment routine as implemented in SPM12 (Statistical Parametric Mapping, Wellcome Department of Imaging Neuroscience, University College London, London, UK) in MATLAB (R2018b, The MathWorks Inc., Natick, MA, 2018). Finally, resulting images cortex segmentation and cortical depth sampling was performed following the same steps as described in the layer-specific structural study (see above).

Extracting microstructural profiles and cortical layer compartments

In the layer-specific structural study, layer-specific qT1, nQSM, pQSM and aQSM values were sampled along 21 cortical depths perpendicular to the cortical sheet. Sampled values were extracted from the five fingertip representations (pRF center location maps), and from the face-hand representation (hand and face activation maps; see section *Localizing body part representations in area 3b*) in area 3b. Layer-specific quantitative values were averaged across vertices within individuals (giving one value per body part and depth). First and second derivatives of layer-specific qT1 profiles were calculated using the gradient function as implemented in MATLAB (R2017b).

The layer-specific structural profiles (including 21 cortical depths) were then further averaged based on a previously introduced approach[14], using *ex-vivo in-vivo* validated myelin profiles of area 3b[16] to identify anatomically-relevant layer compartments in *in-vivo* MRI data (see **Fig. 2B** and **Fig. 2D**). In short, after removing the two deepest layers (where qT1 stabilized) in both age groups, minima and maxima of the first derivative of raw qT1 profiles indicated three data-driven layer compartments: an inner, middle and outer compartment. Based on Dinse et al.[16], we assume that the input layer IV is located in the middle compartment and deep layers V/VI are located in the inner compartment. However, we note that these compartments are based on *in-vivo* MRI data and may therefore not match exactly with the anatomical layers as described by e*x-vivo* myelo- and cytoarchitecture.

Definition of area 3b

In the layer-specific structural study, area 3b was manually delineated based on an operational definition using anatomical landmarks extracted from cytoarchitectonic[94] , fMRI[95] and multimodal parcellation studies[96,97], i.e., following a standardized procedure that has been used previously[7,14,53]. Resulting masks cover the anterior wall of the postcentral gyrus, running from the fundus of the central sulcus to the edge of the rostral bank of the postcentral gyrus (mainly covering area 3b and parts of area 3a). Finally, all masks were plotted in reference to co-registered Freesurfer labels (normalized probabilistic maps of area 3a and area 3b) on the individual cortical surfaces to ensure that the locations of the manual delineations overlap with those outlined by automated approaches (see **Fig. 2-supplemental figure 3**). In the layer-specific functional study, area 3b and the hand area were defined for each individual based on the atlas provided in csurf[98]. This approach was taken because additional, finger-specific functional localizers were used here to detect index and middle finger representations.

Cortical thickness estimation

In the layer-specific structural study, the profile geometry module from the CBS Tools (v3.0.8) was used to calculate overall cortical thickness across cortical depths (after removing the two deepest cortical depths where qT1 values stabilized) and layer-specific cortical thickness of extracted layer compartments.

Functional data preprocessing

In the layer-specific structural study, opposite polarity (PE) EPIs were distortion-corrected using point spread function (PSF) mapping[99]. We applied a weighted image combination to combine the distortion-corrected PE EPIs while controlling for differences in spatial information. Resulting EPIs were motion corrected to time point zero. PSF mapping was performed on motion-corrected EPIs to allow geometrically accurate image reconstruction. Evaluating quality of blocked-design and phase-encoded time series, there were no severe artifacts. Resulting data were slice-time corrected using SPM8 (Statistical Parametric Mapping, Wellcome Department of Imaging Neuroscience, University College London, London, UK). Slice-time corrected data of phase-encoded protocols were concatenated.

In the layer-specific functional study, motion distortion correction was performed using the same method as described for the layer-specific structural study. Data quality was evaluated after acquisition for each participant, and data showing severe artifacts (i.e., n=4 participants) were excluded. Slice timing correction was performed on the remaining

functional data to correct differences between slices during image acquisition using SPM12 (Statistical Parametric Mapping, Wellcome Department of Imaging Neuroscience, University College London, London, UK). Spatial smoothing was performed only to the blocked-design data with 1mm kernel width using SPM12.

Analysis of phase-encoded data

For phase-encoded data, as the time series of different cycle directions (forward or reversed) were mirror-symmetric (see above) to each other, they were averaged time point by time point by reversing the direction of time on a scan-by-scan basis. The time-reversed cycle direction (down➔top cycle) was time-shifted before averaging by 4 seconds (2 TRs) to compensate for hemodynamic delay. Averaging was performed in 3D without any additional registration. Neither normalization nor smoothing was performed on the data during this procedure.

Analysis of blocked design data

In the layer-specific structural study, we used tactile stimulation to localize the hand area in SI. We calculated 1st level fixed-effects models for the two blocked-design runs using a general linear model (GLM) on individual data as implemented in SPM 8. BOLD activation driven by each finger's stimulation was modeled as an independent measure, because each finger was treated individually[100,101]. Five regressors of interest (stimulation to thumb, index, middle, ring, little finger) were modeled per session, resulting in five linear contrasts (e.g., the contrast [-1 4 -1 -1 -1] for stimulation to index finger). Peak clusters of t-values were extracted (p<0.01, minimum cluster size of k=3). Resulting t-value maps were taken forward for surface mapping (see section *Registration and surface mapping of functional data*).

For the motor paradigm, we used the GLM as implemented in SPM 12 to estimate functional activation maps (t-value maps) of tongue and finger movements (first-level analysis using contrast estimates for each body part). We thresholded peak clusters at p<0.01 with a minimum size of k=3 (for details see Northall et al.[7]). Resulting t-maps were taken forward for surface mapping (see section *Registration and surface mapping of functional data*). In participants with congenital limb loss, we used mental imagery of finger movements to locate the hand area in area 3b in the hemisphere contralateral to the missing limb, while the rest of the motor paradigm was equal to the one used for younger and older participants. Again, we used the GLM as implemented in SPM 12 to estimate t-value maps based on contrasts for each body part. We note that the motor paradigm also included movements of the left and right foot (which were not investigated here), resulting in five different contrasts (e.g., the

contrast [1 0 0 0 0] for moving/imagining movements of the left hand). Resulting t-maps were taken forward for surface mapping and were thresholded in surface space (see section *Registration and surface mapping of functional data*).

In the layer-specific functional study, again, we calculated 1st level fixed-effects models for the blocked-design runs using the general linear model (GLM) on individual data as implemented in SPM12. Each finger was treated individually and independently, therefore BOLD activation elicited by each finger's tactile stimulation was treated as an independent measure[5,100,101]. Two regressors of interest were modeled explicitly (stimulation to index finger and stimulation to middle finger) and the rest condition was modeled implicitly. The linear contrast estimate for index and middle finger was computed: F contrast [1 0 / 0 1], replicated for each session. On the individual subject level, voxels that survived a significance threshold of $p<.05$ (uncorrected) were later mapped onto the individual cortical surfaces (see section *Registration and surface mapping of functional data*).

Population receptive field modeling

In the layer-specific structural study, we used the same method as described previously to estimate Bayesian population receptive fields (pRF) of the five fingertips[5,14]. In short, phase-encoded fMRI data were used to perform a two-stage analysis using the BayespRF Toolbox (freely available for download from https://github.com/pzeidman/BayespRF) written for Matlab (SPM12, Matlab R2017b): First, we conducted a 1st level GLM analysis, constructing five regressors for the five fingers of the right hand. Only voxels passing a threshold of $p<.05$ uncorrected were included in pRF modeling[102,103], which was performed on a voxel-by-voxel basis on the inferior-to-superior dimension (x-dimension) of topographic alignment, using a Gaussian response function and a posterior model probability>0.95 (code available for download at https://gitlab.com/pengliu1120/bayesian-prf-modelling.git)[5,102,103]. The analysis was restricted to area 3b to reduce processing time. We extracted pRF center location (x) to locate activated finger-specific voxels (finger-specific ROIs) and pRF width (σ, standard deviation of the Gaussian response function) to estimate the pRF size of activated voxels in one-dimensional stimulus space. The most superficial 20% of the remaining data points were disregarded to minimize the effects of superficial veins.

In the layer-specific functional study, pRF mapping of the index and middle fingers was performed using a Matlab-based toolbox SamSrf v9.4 (free available for download from https://github.com/samsrf/samsrf). The toolbox provides a generic framework to model pRFs with stimulus space in any dimension[104]. The phase-encoding dataset was used here for

pRF mapping, with an additional rest condition to provide baseline information. The forward-order runs and reversed-order runs were first converted into Freesurfer MGH format and projected onto the Recon-all reconstructed surface. Superficial points along the surface normal to each vertex (upper 20% of the cortical thickness) were disregarded to minimize the effect of superficial veins on BOLD signal change. Only the mean value of 20-100% cortical depth was used. After converting from MGH to SamSrf format, the data were concatenated and averaged to increase the signal-to-noise ratio. The data were z-scored and linearly detrended. A stimulus aperture was created to define the somatosensory space. To represent the finger areas that were stimulated during fMRI scanning, the aperture was set up with the dimension of 100×100×320 (320=number of TR). Four finger areas were constructed (two sections in distal phalanx and two sections in intermediate phalanx), with each one associated with each of the stimulation units, based on the stimulation timing. Modeling ROI was defined manually by choosing vertices in the inflated surface model with restricting y-coordinates from -55 to 5 and z-coordinates from 30 to 80 in Freesurfer space, which covered the full SI area. Since the stimulation was applied along one dimension of the fingers, a 2D Gaussian tuning curve vertical model was used to perform the model fitting only on the y-dimension (within-digit dimension), with the x-dimension set as a constant. The receptive field profile is the predicted response for a given location. The predicted time series is convolved with a canonical haemodynamic response function (HRF).

The parameter modeling employed a two-stage coarse-to-fine procedure to obtain the best possible fit of the predicted time series with the observed data. First, a coarse fit process was applied, which involved an extensive grid search by correlating the observed time series against a set of predicted time series derived from a combination of y_0 and σ, covering the plausible range for each parameter. The search space was set at [-1.25 1.25], which covers more than the stimulus space [-1 1]. The parameters giving rise to the maximal correlation can survive and be sent to the second stage. The fine fit is an optimized procedure to refine the parameters by further maximizing the correlation between observed and predicted time series. The noise ceiling was calculated as an estimate of the maximum goodness-of-fit that could theoretically be achieved from the data of each voxel[104], using a similar procedure as Urale et al.[105]. The Spearman-Brown prophecy formula[106] was used to account for the accurate estimate of the true reliability of the time series. Six other parameters were estimated during modeling, including the center location (μ), the sizes (σ), goodness-of-fit (R^2), normalized goodness-to-fit (nR^2), baseline and beta (β). The R^2 is the coefficient of determination of the correlation between the observed and predicted time series, and nR^2 is the normalized coefficient of determination relative to the noise ceiling. During modeling, baseline (intercept) and β parameters (i.e., BOLD response amplitudes) were estimated for

each voxel. After extracting the modeled parameters within the ROI, the resulting data were cleaned by preserving only those vertices with positive β values. The average pRF size (σ) of each condition and of each participant was calculated based on the cleaned data.

%signal change analysis

In the layer-specific structural study, statistical analyses were conducted on the averaged individual time series of the averaged forward- and reversed-order runs from the phase-encoded paradigm[5,100] to calculate mean response amplitudes, using the program Fourier as implemented in csurf (http://www.cogsci.ucsd.edu/~sereno/.tmp/dist/csurf). Discrete Fourier transformations were performed on the time course of each 3D voxel, before calculating the phase and the significance of the periodic activation. Cycles of 20 stimulations were used as input frequencies. Frequencies below 0.005 Hz (known to be dominated by movement artifacts) were excluded, while higher frequencies up to the Nyquist limit (1/2 the sampling rate) were included. For display, a vector was generated whose amplitude was the square root of the F-ratio calculated by comparing the signal amplitude at the stimulus frequency to the signal amplitude at other noise frequencies, and whose angle was the stimulus phase. To estimate mean response amplitudes of the five finger ROIs (in %), we estimated the discrete Fourier transform response amplitude (hypotenuse given real and imaginary values) for each voxel, within each finger's pRF center location area. This value was multiplied by two to account for positive and negative frequencies, again multiplied by two to estimate peak-to-peak values, divided by the number of time points over which averaging was performed to normalize the discrete Fourier transform amplitude, and divided by the average brightness of the functional data set (excluding air). Finally, the value was multiplied by 100 to estimate the percentage response amplitude[5,100]. No spatial smoothing was applied to the data. The data was sampled onto the individual Freesurfer surface for each participant. To minimize the effect of superficial veins on BOLD signal change, superficial points along the surface normal to each vertex (upper 20% of the cortical thickness) were disregarded. The individual maps were calculated based on the mean value of the remaining depths (20-100% cortical depth). Clusters that survived a surface-based correction for multiple comparisons of $p<.05$ (correction was based on the cluster size exclusion method as implemented by surfclust and randsurfclust within the csurf FreeSurfer framework)[107] and a cluster-level correction of $p<.001$ were defined as significant. For each participant and condition, the complex-valued phasing-mapping data (real and imaginary values) was sampled onto the individualized inflated 3D cortical surface, and the values within the ROI were extracted. Mean % signal change of the tactile maps of each condition were calculated.

In the layer-specific functional study, we followed the same process as above, performing the %signal change analysis on the phase-encoding runs (only scans with stimulation cycles were used) for the cross-layer % signal change. There were 8 stimulation cycles for each run, serving as input frequencies. In addition to the above outlined procedure, the complex-valued phasing-mapping data (real and imaginary maps) were registered to the structural MP2RAGE images and segmented into three layer compartments using MIPAV. % signal changes were calculated at each layer compartment for each participant and for each condition.

Resting-state data analysis

In the layer-specific structural study, resting-state functional data were corrected for pulse- and respiration-induced noise. To prepare the physiological data for noise correction and to remove acquisition artifacts, we used the open-source Python-based software 'PhysioNoise'[108]. Resulting respiratory and cardiac phase data were then used to correct the resting-state time series for pulse- and respiration-induced noise by performing RETROspective Image CORrection (RETROICOR)[109] on a slice-by-slice basis[110]. Residuals were taken as cleaned data to regress out motion-related noise parameters (extracted from the raw data) using the program vresiduals as implemented in LIPSIA (freely available for download at: github.com/lipsia-fmri/lipsia)[111]. The resulting data were high-pass filtered at 0.01 Hz (allowing frequencies faster than 0.01 Hz to pass) and smoothed (Gaussian kernel with a FWHM of 2 mm) using the program vpreprocess implemented in LIPSIA. For n=6 participants, physiological data were not successfully recorded due to loosening the pulse oximeter and/or breathing belt during scanning, which interrupted successful data sampling. For n=5 participants, severe motion artifacts were detected in the resting-state data. Therefore, resting-state analyses are presented for n=29 (14 younger, 15 older) participants only.

Eigenvector centrality (EC) maps were calculated in native space as a measure of network centrality (i.e. maps of functional network hubs) using the program vecm, implemented in LIPSIA[111]. Thereby, the method of rectified linear unit correlation (RLC)[112] was applied, which is suitable for high-resolution fMRI data.

Registration and surface mapping of functional data

In the layer-specific structural study, all functional data were registered to the qT1 image using the automated registration tool in ITK-SNAP (version 3.6.0, non-rigid transformation, 9 degrees of freedom). Manual refinement was applied where required to ensure registration

accuracy. Registration matrices were applied to statistical maps (i.e., t-maps, pRF maps, Eigenvector centrality maps) in a single step (ANTs, version 2.1.0, nearest neighbor interpolation). We note that all ROI analyses were performed on non-smoothed functional data (in original individual space) before statistical maps were registered to individual structural data space. Area 3b masks were applied to all functional data. Registered individual functional parameter maps (e.g., t-value maps, pRF maps, EC maps) were mapped onto the individual cortical surfaces (method of closest point)[81]. The most superficial 20% of cortical values were excluded (to account for superficial veins affecting the BOLD signal). The mean of the remaining cortical values (covering 20-100% of cortical depth) were used to compute statistics independent of cortical depth.

In the layer-specific functional study, for layer-specific analyses, functional time series (i.e., resting state data, blocked-design data, phase-encoded data) were registered to the MP2RAGE image using ANTs (v2.1.0, nearest neighbor interpolation). The resulting registration matrices were applied to the corresponding functional parameter maps (i.e., GLM estimates for localiser images and fourier transform estimates). For cross-layer functional analyses, functional volumes were registered to the T1-weighted 3D MPRAGE image (same image used for recon-all brain segmentation) using csurf tkregister (12 degrees of freedom, non-rigid registration). And the x, y and z location of each surface vertex was mapped into functional voxel coordinates with the obtained registration matrix. The floating point coordinates of points at varying distances along the surface normal to a vertex were used to perform nearest neighbor sampling of the functional volume voxels (i.e., the 3D functional data were associated with each vertex on the surface by finding which voxel that point lay within).

Localizing body part representations in area 3b

In the layer-specific structural study, pRF center location maps (restricted to area 3b) served as localizer for individual finger representations. A “winner-takes-it-all” approach was applied to sample vertices only once. Overlapping vertices (introduced by mapping splitted single finger pRF center location maps) were exclusively assigned to the finger map with the highest variance (explained by pRF modeling). Combining the five single finger maps to one ROI defined the hand area in area 3b of younger and older adults.

Hand and face activation maps resulting from the motor paradigm were used to localize the hand-face area in younger and older adults and in the participant with congenital arm loss. A “winner-takes-it-all” approach was applied to the extracted values to sample vertices only

once. For the participant with congenital arm loss, the lowest 30% of t-values were removed to ensure comparable map sizes within and between participants. To exclude spatial outliers, vertices located more than two standard deviations away from the location of the main cluster (in z-direction and in y-direction) were removed from the final data.

In the layer-specific functional study, the functional representations of each finger were localized based on the pre-processed blocked-design data (see section *Analysis of blocked design data*). Thresholded parameter maps were mapped onto individual surfaces generated by csurf. The overlapping area between the hand area[98] and the index and middle finger representation in area 3b of each individual was used as ROI for phase-encoding analyses and pRF modeling.

Automatic detection of low-myelin borders

To investigate low-myelin borders in human area 3b in the *layer-specific structural study*, a multimodal surface-based mapping approach was applied to each individual dataset[14]. First, multidimensional sampling (inferior to superior, anterior to posterior) of layer-specific qT1 values was performed within area 3b (Pyvista implementation of the Dijkstra algorithm[113]). The peak activation of the thumb (as identified by blocked design data) served as seed region to sample geodesic paths in inferior-to-superior direction, connecting the upper face representation with the little finger representation. Start and end points were defined along the y-axis of D1 and D5 activation peaks and 10 mm (geodesic distance on shortest path) below the D1 activation peak (estimation based on the location of the forehead as described previously[114]). Considered vertices were scattered within one vertex-to-vertex distance of appr. 0.28 mm around the y-axis. Only in cases where the underlying qT1 pattern did not match y-axis sampling, start and end points were defined along the x-axis. Five equally-distant geodesic paths were sampled for each participant (see **Fig. 2-supplemental figure 2A**) to extract qT1 values from middle cortex depth (where the detection of low-myelin borders in area 3b is expected based on previous findings[13]). Second, peak detection was performed on the five extracted qT1 signals (see **Fig. 2-supplemental figure 2A**). To control for a possible gradient in cortical myelin content along the inferior-to-superior axis[13], all qT1 signals were detrended before the *find_peaks* algorithm from the SciPy signal processing toolbox (version 1.10.1) was applied to find the most prominent peaks (local maxima with a prominence > 2 SD from the mean of absolute detrended qT1 values) in each detrended qT1 signal by comparing neighboring values. Resulting peaks were considered a low-myelin border (reflected by a row of high qT1 values) when they occurred in at least 3/5 detrended qT1 signals based on a nearest neighbor approach. The nearest peaks on first and second

neighbor signals were grouped together based on geodesic distances. Peaks with a geodesic distance < 5 mm were considered near. Third, resulting low-myelin borders were back-projected to individual cortical surfaces and visualized in reference to individual pRF finger maps to categorize low-myelin borders in hand-face borders and within-hand borders (i.e., by visual inspection). Finally, a number of different features were extracted for each peak including prominence, full width at half maximum, qT1 intensity, Eigenvector centrality, signed QSM intensity, nQSM intensity, pQSM intensity and aQSM intensity. For each feature, all values belonging to a single border were averaged to obtain one feature vector for each border. Feature vectors of within-hand borders were further averaged across all within-hand borders. In this way, we extracted two feature vectors (one for within-hand borders and one for the hand-face border) in each individual which were used to calculate group statistics (between younger and older adults).

Statistical analyses of MRI data

In the layer-specific structural study, all statistical analyses were carried out in R (version 4.2.2, R Core Team, 2022). All sample distributions were analysed for outliers using boxplot methods and tested for normality using Shapiro-Wilk's test. Homogeneity of variances was tested with Levene's test. We applied two-sided tests. The significance level was set to p=0.05. Bonferroni-corrected significance levels were applied for multiple testing to correct for familywise error accumulation. To account for skewed and heteroscedastic data), we calculated robust permutation tests[115,116]. Group differences between younger and older adults (i.e., cortical thickness and septa analyses) were investigated with independent-samples random permutation Welch t-tests (100k Monte-Carlo permutations, two-sided, equal-tail permutation *p*-value) using the MKinfer package (version 1.1, https://cran.r-project.org/package=MKinfer). To investigate interaction effects between the factors age (between-subjects factor, levels: younger, older) and layer (within-subjects factor, levels: outer, middle, inner) as well as between the factors, age, layer and body-part (with-subjects factor, levels: thumb, index, middle, ring, little finger, or levels: hand, face) we calculated mixed-effects permutation ANOVAs (type III) using the "Rd_kheradPajouh_renaud" method for random effects models as implemented in the permuco package (version 1.1.2)[117] written for R (version 4.2.2, R Core Team, 2022). The number of permutations was set to 100000. For comparability reasons we report both, results of parametric mixed-effects ANOVAs (using Greenhouse-Geisser corrected degrees of freedom and p-values in case of sphericity violations) and non-parametric permutation mixed-effects ANOVAs. Generalized eta squared (η_G^2) was calculated as an effect size estimator for parametric ANOVAs. To follow-up significant interaction effects, we calculated

Welch t-tests using bootstrapped samples to estimate confidence intervals and p-values (as implemented in the MKinfer package version 1.1)[118], accounting for non-normality in underlying conditions. For comparability we report both results, i.e., with and without bootstrapping. To regress out the effect of map size on layer-specific structural values, we calculated group-wise linear regression models using the lme 4 package (version 1.1.33) while controlling for the effect of individuals (random intercept model, e.g. middle qT1 ~ map size + 1/participant). Intercepts were re-added to the resulting residuals before they were taken forward for between-finger and hand-face comparisons.

The JASP software package (Version 0.17.1, JASP Team, 2023) was used to calculate Bayesian independent-sample t-tests for each stimulation condition on % signal change and pRF size (σ) to compare younger with older adults. Mann-Whitney tests with 5 chains of 1000 iterations were used when data were not normally distributed. The choice of priors (Cauchy, scale=0.707) and the Markov chain Monte Carlo settings were the default as implemented in JASP (for all Bayesian tests)[119,120]. Following the JASP user manual, the Bayes Factor (BF) can be interpreted as follows: BF=1-3 anecdotal evidence, BF=3-10 moderate evidence and BF=10-30 strong evidence[121].

Behavioral measurements

Layer-specific structural study

Tactile Detection Task

Tactile detection of touch to the surface of the fingertip was assessed using fine hair stimuli. We used a subset (0.008 g, 0.02 g, 0.04 g, 0.07 g, 0.16 g, 0.4 g, 0.6 g, 1.0 g, 1.4 g, 2.0 g, 4.0 g, 6.0 g) of standardized tactile monofilaments (Semmes-Weinstein monofilaments; Baseline, Fabrication Enterprises Inc., White Plains, NY, USA) to apply different mechanical forces to the skin surface of the fingertips (see **Fig. 1**). Stimuli were manually applied to a predefined skin area (circle with a diameter of approximately 2 mm), touching the skin surface at an angle of approximately 90 degree, for one second[122]. Stimulus application was guided by auditory instructions via headphones which were controlled by the Psychophysics Toolbox extension[123,124] in MATLAB (R2017b). All participants sat in front of a screen that signaled the beginning and ending of stimulus intervals and listened to white noise via headphones. The right hand (palm facing upwards) was fixated on a small pillow behind a paper wall, preventing participants from seeing their own hand and the experimenter.

In a two-alternative forced choice paradigm, participants chose one of two possible time intervals that contained the stimulation (randomly applied in the first or second interval)[125,126]. Application of tactile monofilaments followed a 3-down/1-up staircase approach with two interleaved staircases, one starting at a weight of 0.02 gram and the other starting at a weight of 0.4 gram. The stimulus weight was increased by one step after each error, and decreased by one step after every three correct responses, until stable performance was reached[125]. This procedure was separately applied for each of the two staircases[127]. The experiment was finished when for the last 30 trials the standard variation in stimulus intensity was 1 step or less[125], or when the maximum number of 100 trials was reached. The participant‘s tactile detection threshold was defined as the mean stimulus intensity across reversal points (change of response from correct to incorrect or incorrect to correct) within the period of stable performance (i.e., the last 10 trials)[126]. The experiment took approximately 12 min per finger.

Before averaging, stimulus intensities were transformed logarithmically on a 1/10th milligram scale (log 10 0.1mg), yielding approximately equal intervals between filaments. Lower values indicate higher tactile sensitivity to mechanical forces. Additionally, we estimated the skin indentation in mm based on the examined detection threshold. Detection thresholds were taken as proxies of corresponding values in milliNewton (mN) that were provided by the manufacturer. Afterwards, the skin indentation δ was calculated according to the following equation[128]:

$$\delta = [(F/A)\,(1/b)\,] * \hat{\delta}$$

F is the estimated force in Newton (N), A (=0.2368 N) and b (=2.0696) are material/structural constants and $\hat{\delta}$ (=1.00 mm) is the reference indentation[128]. Finally, the result (δ) was multiplied by 3 to get an indentation value clearly above threshold, which was used to increase the amplitude of pin movement in the 2PD task. All calculations were performed in Matlab (R2017b).

Finger Discrimination Task

Again, Semmes Weinstein monofilaments were used to apply tactile stimulation, targeting the same stimulation sites as described for the tactile detection task. In a five-alternative-forced-choice design, tactile stimulation (lasting 1 second) was applied to one of five possible fingertips. Participants were asked to name the finger where they felt the touch. Answers were given verbally within a limited response interval (lasting 7 seconds). In case participants perceived no touch (note that tactile stimulation was applied at individual

detection thresholds and was therefore expected to be perceived only in approximately 50% of the cases), they were motivated to guess. Each fingertip was stimulated 20 times, using unique pseudo-randomized sequences (with fingertips being stimulated not more than two times in a row). To extract the finger discrimination sensitivity (sensitivity of one finger being correctly discriminated from other fingers), we applied signal detection theory and calculated the d-prime as bias-free index of discrimination sensitivity[129,130] by computing the amount of times a specific finger was touched and detected (hit), or was not touched but falsely detected (false alarm). Hits and false alarms were first converted to z-scores before subtracting false alarms from hits. D-primes were obtained for each finger separately.

2-Point Discrimination Task (2PD Task)

We assessed the tactile discrimination performance of the right index finger[3,131,132]. Stimulation was applied by two rounded pins (diameter=0.4 mm) simultaneously touching the surface of the fingertip. A custom-made, fully automatic stimulation device moved the pins up and down, controlled by the software package Presentation (version 16.5, Neurobehavioral Systems, Inc., Albany, CA, USA). The amplitude of pin movement was adjusted to the individual detection threshold (as assessed before in the tactile detection task), but was at least set to 1.2 mm. Spacing between pins ranged from 0.7 to 2.8 mm (in steps of 0.3 mm) for younger adults and from 0.7 to 6.3 mm (in steps of 0.8 mm) for older adults. Additionally, a single pin was included as control condition. Pin spacing was vertically adjusted by rotating a disc containing all possible pin spacing conditions (n=9). In a two-alternative forced-choice paradigm, pin spacing conditions were pseudo-randomly presented. Participants indicated whether they perceived one or two single pins touching their fingertip. They were instructed to give the answer ‘two pins felt’ only if they were certain. The right index finger was fixated on the stimulator, and the hand was covered by a white box during the task to prevent effects caused by seeing the stimulated finger[133,134]. Each task block included 90 trials (10 repetitions per pin condition). To prevent order effects, unique sequences of pin spacing conditions were used per participant and run. All participants completed two runs. Intertrial intervals were pseudo-randomized and varied between 1 to 5 seconds. 2PD thresholds were calculated per participant and run. Answers “two pins felt” were fitted as percentages across ascending pin distances (0.7-2.8 mm). A binary logistic regression was used to fit the data using the glmfit function (iterative weighted least square algorithm) from the Statistics Toolbox as implemented in MATLAB R2017b). The 2PD threshold was taken from the pin distance where the 50 percent level crossed the fitted sigmoid curve[131,132,135,136]. Lower values indicate higher spatial acuity.

Z-transformed false alarm and hit rates were calculated for each participant to derive d-prime values as bias-free indices of 2PD sensitivity. Hit rates were calculated as the proportion “2 pins felt” responses when the stimulus consisted of two pins. False alarm rates were calculated as the proportion “2 pins felt” responses when the stimulus consisted only of one pin. False alarm rates were adjusted to 0.1 by default, if no false alarm was detected[131].

Precision Grip Task

Sensorimotor integration performance was assessed with a custom made pressure sensor that was held between the thumb and index finger of the right hand, adjusted to individual strength (see **Fig. 1**)[137]. Reference forces that were to be matched ranged from 5% to 25% of the individual maximum grip force to avoid muscle fatigue[138]. Participants solved a visuo-motor matching task[137,139], demanding them to continuously adjust the grip force. Applied forces were sampled at a frequency of 100 Hz and projected on screen at a refresh rate of 60 Hz. The task was controlled by the software package Presentation (version 16.5, Neurobehavioral Systems, Inc., Albany, CA, USA). Each task repetition contained a unique pseudo-randomized sequence of 10 position changes at five different amplitudes (5%, 10%, 15%, 20%, 25% of maximum grip force), leading to a mean frequency of 0.25 Hz. After a period of task familiarization[138,139], all participants performed the task for a total duration of 20 seconds. One run contained 15 trials divided by intertrial intervals of 10 seconds, leading to a total duration of about 8 minutes per run. All participants performed two runs that were separated by a 5-minute resting period. After each trial, participants received feedback about their individual performance level on screen. We monitored the time (in seconds) the controllable bar was within a given percentage above (2.5%) and below (2.5%) the target line (upper edge of the reference bar)[137,138]. Higher values reflect better sensorimotor integration.

Layer-specific functional study

Tactile detection task

We measured the tactile threshold of the index and middle finger of the right hand. During testing, participants were asked to sit on a chair with the right hand positioned on a custom-build, metal-free applicator with an independently-controlled MR-compatible piezoelectric stimulator (same device used during fMRI task) set underneath the tested finger. The tested hand was occluded from view. The tactile threshold was detected with a two-alternative forced task. At each trial, two intervals were presented with only one of them containing a stimulation, which was one pin rising up during a stimulation with a certain amplitude, lasting for 1 second. Participants were asked to detect the stimulation interval by

pressing the respective key on the keyboard in a self-paced manner ("1" or "2"). A randomized sequence (different for each participant) was used to determine which interval contained the stimulation. The adaptive thresholding procedure followed a 3-down/1-up staircase algorithm. For each finger, the stimulation amplitude started at 0.73 mm. Every time the participant chose the correct interval three times in a row, the amplitude went down for 0.03 mm, whereas if the participant chose the wrong interval, the amplitude went up for 0.03 mm. There were 30 trials to start with, and the participants were expected to reach an accuracy above 80%. If the accuracy was below 80%, there would be more trials until the accuracy reached the requirement. The task took approximately 45 to 60 minutes.

Texture roughness discrimination

The texture roughness discrimination test was used to detect individual tactile sensation of surface roughness. The test comprises a plastic board with 15 columns, and the size of each column is 1.0×1.5 cm. Each column consists of small pins arranged with densities at different levels, resulting in a roughness ranking from rough (level 1) to smooth (level 10). During testing, participants were asked to sit on a chair with the arm positioned on a foam cushion. The tested hand was occluded from view. At each trial, two intervals were presented containing stimulation with two different roughness stimuli. Participants were asked to detect the column with higher roughness (i.e., less density). They were asked to press the respective key on the keyboard in a self-paced manner ("1" or "2"). For stimulus application, the experimenter followed auditory instructions via headphones. Neither the hand nor the experimenter were visible to the participant during testing. The plastic board was positioned under the participants' right hand during the stimulation and withdrawn afterwards. The test was composed of two conditions, each included 30 trials. During the first testing condition, the tactile sensation of the index finger was tested and during the second testing condition, the tactile sensation of index and middle finger combined was tested. The stimulation pairs were chosen under three different conditions, with the roughness level increasing consecutively (e.g., level 3 and level 4) or in increments of two (e.g., level 3 and level 5) or three (e.g., level 3 and level 6). Stimulation pairs too easy or too difficult to distinguish were excluded. The stimulation order for each pair and for the sequence were randomized for each participant. The test took approximately 45 to 60 minutes.

Hand dexterity

Two standard tests (i.e., the Grooved Pegboard Test and The O'Conner Finger Dexterity Test) were used to test individual levels of hand motor function[5,7,131], each consisting of two conditions. During one testing condition, participants were asked to only use their thumb and

index finger of the right hand, whereas during the other testing condition, they were asked to use thumb, index finger and middle finger.

We also performed the Small Motor Test. It was employed to explore the haptic object sensation and coordinated motor movement function, which also consisted of two conditions. During one testing condition, participants were asked to only use their thumb and index finger of the right hand to pick up the pins, whereas during the other testing condition, they can use thumb, index finger and middle finger. It was composed of hexagonal-shaped nuts and small metal pins. The task was to pick up a pin using two fingers or three fingers to fill in the hole on a hexagonal-shaped nut held by the left hand, after success then move on to the next pair. As there is no requirement on how they could hold the nut with the left hand, it requires coordinating fingers of the right hand for holding the pin, and coordinating both left and right hand to aim for the hole. We measured the number of pins and nuts that were successfully paired with each other (n).

Statistical analyses of behavioral data

In the layer-specific structural study, all behavioral measures (tactile detection thresholds, 2PD thresholds and 2PD sensitivity, finger discrimination sensitivity, precision grip accuracy) and functional outcome variables (% signal change, network centrality) were compared between age groups using independent-samples random permutation Welch t-tests (100k Monte-Carlo permutations, two-sided, equal-tail permutation *p*-value) as implemented in the MKinfer package (version 1.1) for R (version 4.2.2, R Core Team, 2022).

Tactile detection thresholds and 2PD sensitivity of the right index finger, precision grip accuracy (i.e. sensorimotor integration) involving both the right thumb and the right index finger as well as % signal change (i.e. responsivity) and network centrality (i.e. EC) of the contralateral index finger representation were correlated with layer-specific qT1 values of the contralateral index finger representation. Correlation analyses were performed using Kendall's tau correlation coefficient. Uncorrected results are reported. Before calculating correlations, the data was partly transformed (using the reciprocal of tactile detection thresholds and qT1 values), so that in the final scatterplots higher values always indicate better performance in behavior, higher responsivity, and more connectivity in fMRI markers, as well as higher substance concentration in structural MRI markers. Regression lines in the scatterplots (**Fig. 6**) were generated based on robust linear Theil-Sen regression estimates[36], because the estimation of the regression coefficients is based on Kendall's tau[37]. Cut-offs for the interpretation of Kendall's tau correlation coefficients were

approximated with the following equation, where r denotes the Pearson correlation coefficient[38]:

$$tau = 2/\pi \, arcsin(r)$$

To derive the cut-off values, we applied the equation to a previously stratified convention for the Pearson correlation coefficient[39].

In the layer-specific functional study, behavioral statistics included data of 21 healthy younger adults and 17 healthy older adults. Nonparametric independent sample Mann-Whitney U tests were used to compare texture roughness and hand dexterity measures between age groups. Effect sizes are given by the rank biserial correlation.

The functional signal central peak at layer IV of the index finger and double-finger (index and middle finger together) representation were correlated with the texture roughness discrimination accuracy, the number of holes filled in the Grooved Pegboard Test and the number of pairs completed in the Small Motor Test for the index finger and the double finger condition, respectively. Correlation analyses were performed using Kendall's tau correlation coefficient. Uncorrected results are reported.

Mice

Experiments were performed in young (4-5 months; n=8) and old (14-20 months; n=8) mice in both male and female transgenic mice expressing genetically encoded calcium indicators (GCaMP6f; C57BL/6J-Tg (Thy1-GCaMP6f) GP5.5Dkim/J; RRID: IMSR_JAX:024276). Mice were housed in standard cages at a 12 h/12 h light dark cycle, food and water were provided ad libitum. All experiments were performed according to the NIH Guide for the Care and Use of Laboratory animals (2011)[140] and the Directive of the European Communities Parliament and Council on the protection of animals used for scientific purposes (2010/63/EU) and were approved by the animal care committee of Sachsen-Anhalt, Germany.

Cranial window

For cranial window implantation, mice were anesthetized with isoflurane (4% for induction and 2% maintenance during surgery). Eye cream was applied to protect the eyes (Bepanthen, Bayer), analgesics and anti-inflammatory drugs were injected subcutaneously (carprofen, 0.15 mg, and dexamethasone, 2 mg). After shaving and disinfection of the scalp, a section of skin was removed. A craniotomy was then made over the left S1-barrel field, the window was 3 mm in diameter. A glass coverslip was then placed on top of the craniotomy

and fixed with glue (gel control, Loctite). A custom-built headplate was implanted on the exposed skull with glue and cemented with dental acrylic (Paladur, Heraeus Kulzer).

Two-photon calcium imaging

Two-photon calcium imaging was performed using an 8 kHz resonant scanning microscope (HyperScope, Scientifica) with an Ultrafast laser (InSight X3 Dual output laser; Spectra-Physics; <120 fs pulse width, 80 MHz repetition rate) tuned to 940 nm. Images were acquired at 30 Hz (using a 16X objective 0.8 NA, Nikon; tilted 10° from vertical for S1-barrel field imaging with ScanImage software (Vidrio Technologies). Imaging of layer II/III S1-barrel field was performed at cortical depths between 150–250 µm and layer 5 imaging between 420-550 µm, each FOV was imaged under 3 whisker stimulation conditions (see **Fig. 1C**). For all imaging sessions, mice were awake, head restrained, and placed on an air-suspended polystyrene 20 cm ball (Jet Ball system, PhenoSys GmbH, sampling frequency 30 Hz). The sampling frequency of the calcium imaging was resampled to precisely match the sampling frequency of the optical encoders, sensory stimulation and behavioral readouts. Whisker stimulation was performed by an implemented air puff system (PhenoSys GmbH). Animals were in the dark for all trials.

Whisker stimulation

All three stimulation conditions consisted of randomized airpuffs directed to the right side whiskers and two-photon imaging performed in the left barrel field. Two fields-of-view were imaged for each mouse under each whisker stimulus condition, one in the outer layers (layer II/III) and one in the inner layers (layer V). First, all whiskers were stimulated (all whisker condition); after trimming the whiskers except for only two whiskers remaining on the right whisker pad (two of D1-D4 whiskers) the second session was performed (two-whisker condition; W1+W2), and after trimming one of the remaining two whiskers the last session of stimulating was performed (one whisker condition; W1). The stimulation protocol consisted of ~30 airpuffs (200 ms duration) delivered at randomized inter-stimulus intervals (range 6-20 seconds) for each field-of-view flanked by 2 minutes imaging of spontaneous activity (10 min total).

Histology

Animals were deeply anesthetized with ketamine (20 mg/100 g body weight, ip) and xylazine (1 mg/100 g body weight, ip) and perfused transcardially with 20 mL of 0.1 M phosphate-buffered saline (PBS, pH 7.4) followed by 200 mL of 4% paraformaldehyde. The

brains were extracted, post-fixed overnight in 4% paraformaldehyde at 4°C, and then cryoprotected in 30 % sucrose in PBS for 48 h. Brains were cut into 50 µm thick coronal sections (CryoStar NX70, Thermo Scientific, USA) and collected in PBS (free-floating). For immunohistochemistry, serial series of floating sections were then blocked in normal donkey serum (10 % and 0.4 % triton in PBS) for 1 h and incubated in primary antibodies overnight at 4°C to visualize parvalbumin (PV; monoclonal mouse anti-parvalbumin, 1:4000, Swant, PV 235; RRID: AB_10000343). After rinsing in PBS, sections were incubated for 2 h with donkey anti-mouse Cy3 (Jackson ImmunoResearch Labs Cat# 715-165-150, RRID: AB_2340813, United Kingdom). Finally, sections were rinsed again in PBS, mounted on gelatin-coated slides, and coverslipped with mounting media containing DAPI (4′,6-diamidino-2-phenylindole) counterstain (Vectashield). High resolution images were captured using an epifluorescence microscope (Keyence, Japan) under a 10x objective and merged (resulting in a ~15000 × 11000 pixel image per coronal section).

Data analysis

Two-photon calcium imaging datasets (30Hz) were motion corrected and cell detection and signal extraction performed using Suite2p[141]. To calculate the change in fluorescence (ΔF/F), the pixel intensity is averaged within each ROI, representing the change in intensity for a single neuron, to create a raw fluorescence time series F(t). Baseline fluorescence F0 was computed for each neuron by taking the 5th percentile of the smoothed F(t) (1 Hz lowpass, zero-phase, 60th-order FIR filter) and the change in fluorescence relative to baseline (ΔF/F0) was calculated (F(t)-F0/F0). We used nonnegative matrix factorization (NMF), in order to remove neuropil contamination as implemented in FISSA[142]. All further analyses were performed using custom-written scripts in MATLAB (MathWorks, MA, USA). Histological analysis was performed on 3 representative sections of a 1 mm medio-lateral extent for each brain across the entire cortical depth. Representative sections were taken throughout the anterior-posterior extent of the barrel field and images were aligned to the cortical depth matching the surface, layer IV and the ventral white matter border as demarcated by DAPI. DAPI staining was also used to demarcate the cortical layers in the aligned images, namely outer layers, supragranular (I/II/III); middle layers, granular (IV); and inner layers, infragranular (V/VII) of the barrel cortex (using Fiji, ImageJ software)[143]. Cells were then automatically counted using the open-source software cellpose[144] with the nuclei model (DAPI) and Cyto model (PV neurons). Cell density was then calculated by normalizing to the area for the given demarcated cortical depths for each layer and across the given anterior posterior sections.

Author contribution

Conceptualization: E.K., P.L., J.D., J.M.P.P.

Methodology: P.L., J.D., E.K., J.M.P.P., J.U.H., D.S.S.

Formal Analysis: P.L., J.D., J.M.P.P., J.U.H.

Investigation: P.L., J.D., E.K., J.M.P.P

Writing - original draft preparation: P.L., J.D., J.M.P.P., J.U.H.

Writing - review and editing: P.L., J.D., E.K., J.M.P.P., J.U.H., D.S.S., O.S

Visualization: P.L., J.D., J.M.P.P., J.U.H.

Supervision: E.K., J.M.P.P.

Funding acquisition: E.K., J.M.P.P., O.S.

All authors contributed to the article and approved the submitted version.

Competing interests

No competing interests to declare.

References

1. Stacho, M. *et al.* A cortex-like canonical circuit in the avian forebrain. *Science* **369**, eabc5534 (2020).
2. Barnes, C. A., Rao, G. & McNaughton, B. L. Increased electrotonic coupling in aged rat hippocampus: A possible mechanism for cellular excitability changes. *J. Comp. Neurol.* **259**, 549–558 (1987).
3. Pleger, B. *et al.* A complementary role of intracortical inhibition in age-related tactile degradation and its remodelling in humans. *Sci. Rep.* **6**, 27388 (2016).
4. Popescu, I. R. *et al.* Increased intrinsic excitability and decreased synaptic inhibition in aged somatosensory cortex pyramidal neurons. *Neurobiol. Aging* **98**, 88–98 (2021).
5. Liu, P. *et al.* The organizational principles of de-differentiated topographic maps in somatosensory cortex. *eLife* **10**, e60090 (2021).
6. Calì, C. *et al.* The effects of aging on neuropil structure in mouse somatosensory cortex—A 3D electron microscopy analysis of layer 1. *PLOS ONE* **13**, e0198131 (2018).
7. Northall, A. *et al.* Layer-specific vulnerability is a mechanism of topographic map aging. *Neurobiol. Aging* **128**, 17–32 (2023).
8. Barrera, K. *et al.* Organization of myelin in the mouse somatosensory barrel cortex and the effects of sensory deprivation. *Dev. Neurobiol.* **73**, 297–314 (2013).
9. Verdú, E., Ceballos, D., Vilches, J. J. & Navarro, X. Influence of aging on peripheral nerve function and regeneration. *J. Peripher. Nerv. Syst.* **5**, 191–208 (2000).
10. Clarey, J. C., Tweedale, R. & Calford, M. B. Interhemispheric Modulation of Somatosensory Receptive Fields: Evidence for Plasticity in Primary Somatosensory Cortex. *Cereb. Cortex* **6**, 196–206 (1996).
11. Peters, A., Sethares, C. & Luebke, J. I. SYNAPSES ARE LOST DURING AGING IN THE PRIMATE PREFRONTAL CORTEX. *Neuroscience* **152**, 970–981 (2008).
12. Lenz, M. *et al.* Increased Excitability of Somatosensory Cortex in Aged Humans is Associated with Impaired Tactile Acuity. 6 (2012).

13. Kuehn, E. *et al.* Body Topography Parcellates Human Sensory and Motor Cortex. *Cereb. Cortex* **27**, 3790–3805 (2017).

14. Doehler, J. *et al.* The 3D Structural Architecture of the Human Hand Area is Non-Topographic. *J. Neurosci.* JN-RM-1692-22 (2023) doi:10.1523/JNEUROSCI.1692-22.2023.

15. O'Connor, D. H., Krubitzer, L. & Bensmaia, S. Of mice and monkeys: Somatosensory processing in two prominent animal models. *Prog. Neurobiol.* **201**, 102008 (2021).

16. Dinse, J. *et al.* A cytoarchitecture-driven myelin model reveals area-specific signatures in human primary and secondary areas using ultra-high resolution in-vivo brain MRI. *NeuroImage* **114**, 71–87 (2015).

17. Sui, Y. V., Masurkar, A. V., Rusinek, H., Reisberg, B. & Lazar, M. Cortical myelin profile variations in healthy aging brain: A T1w/T2w ratio study. *NeuroImage* **264**, 119743 (2022).

18. Fischl, B. & Dale, A. M. Measuring the thickness of the human cerebral cortex from magnetic resonance images. *Proc. Natl. Acad. Sci.* **97**, 11050–11055 (2000).

19. Fjell, A. M. *et al.* What is normal in normal aging? Effects of aging, amyloid and Alzheimer's disease on the cerebral cortex and the hippocampus. *Prog. Neurobiol.* **117**, 20–40 (2014).

20. Salat, D. H. *et al.* Thinning of the Cerebral Cortex in Aging. *Cereb. Cortex* **14**, 721–730 (2004).

21. Kikkert, S. *et al.* Revealing the neural fingerprints of a missing hand. *eLife* **5**, e15292 (2016).

22. Yu, Y. *et al.* Layer-specific activation in human primary somatosensory cortex during tactile temporal prediction error processing. *NeuroImage* **248**, 118867 (2022).

23. Yu, Y. *et al.* Layer-specific activation of sensory input and predictive feedback in the human primary somatosensory cortex. *Sci. Adv.* **5**, eaav9053 (2019).

24. Stüber, C. *et al.* Myelin and iron concentration in the human brain: A quantitative study of MRI contrast. *NeuroImage* **93**, 95–106 (2014).

25. Hametner, S. *et al.* The influence of brain iron and myelin on magnetic susceptibility and effective transverse relaxation - A biochemical and histological validation study. *NeuroImage* **179**, 117–133 (2018).

26. Langkammer, C. *et al.* Quantitative susceptibility mapping (QSM) as a means to measure brain iron? A post mortem validation study. *NeuroImage* **62**, 1593–1599 (2012).

27. Zheng, W., Nichol, H., Liu, S., Cheng, Y.-C. N. & Haacke, E. M. Measuring iron in the brain using quantitative susceptibility mapping and X-ray fluorescence imaging. *NeuroImage* **78**, 68–74 (2013).

28. Betts, M. J., Acosta-Cabronero, J., Cardenas-Blanco, A., Nestor, P. J. & Düzel, E. High-resolution characterisation of the aging brain using simultaneous quantitative susceptibility mapping (QSM) and R2* measurements at 7T. *NeuroImage* **138**, 43–63 (2016).

29. Acosta-Cabronero, J., Betts, M. J., Cardenas-Blanco, A., Yang, S. & Nestor, P. J. *In Vivo* MRI Mapping of Brain Iron Deposition across the Adult Lifespan. *J. Neurosci.* **36**, 364–374 (2016).

30. Callaghan, M. F. *et al.* Widespread age-related differences in the human brain microstructure revealed by quantitative magnetic resonance imaging. *Neurobiol. Aging* **35**, 1862–1872 (2014).

31. Kuehn, E., Mueller, K., Turner, R. & Schütz-Bosbach, S. The functional architecture of S1 during touch observation described with 7 T fMRI. *Brain Struct. Funct.* **219**, 119–140 (2014).

32. Ruben, J. *et al.* Subarea-specific Suppressive Interaction in the BOLD Responses to Simultaneous Finger Stimulation in Human Primary Somatosensory Cortex: Evidence for Increasing Rostral-to-caudal Convergence. *Cereb. Cortex* **16**, 819–826 (2006).

33. Chen, T.-W. *et al.* Ultrasensitive fluorescent proteins for imaging neuronal activity. *Nature* **499**, 295–300 (2013).

34. Dana, H. *et al.* Thy1-GCaMP6 transgenic mice for neuronal population imaging in vivo.

PloS One **9**, e108697 (2014).

35. Rudy, B., Fishell, G., Lee, S. & Hjerling-Leffler, J. Three Groups of Interneurons Account for Nearly 100% of Neocortical GABAergic Neurons. *Dev. Neurobiol.* **71**, 45–61 (2011).
36. Theil, H. A Rank-Invariant Method of Linear and Polynomial Regression Analysis. in *Henri Theil's Contributions to Economics and Econometrics: Econometric Theory and Methodology* (eds. Raj, B. & Koerts, J.) 345–381 (Springer Netherlands, 1992). doi:10.1007/978-94-011-2546-8_20.
37. Sen, P. K. Estimates of the Regression Coefficient Based on Kendall's Tau. *J. Am. Stat. Assoc.* **63**, 1379–1389 (1968).
38. Kendall, M. G. Rank and Product-Moment Correlation. *Biometrika* **36**, 177–193 (1949).
39. Schober, P., Boer, C. & Schwarte, L. A. Correlation Coefficients: Appropriate Use and Interpretation. *Anesth. Analg.* **126**, 1763 (2018).
40. Micheva, K. D. & Beaulieu, C. An anatomical substrate for experience-dependent plasticity of the rat barrel field cortex. *Proc. Natl. Acad. Sci.* **92**, 11834–11838 (1995).
41. Muret, D. & Makin, T. R. The homeostatic homunculus: rethinking deprivation-triggered reorganisation. *Curr. Opin. Neurobiol.* **67**, 115–122 (2021).
42. Vidal-Pineiro, D. *et al.* Cellular correlates of cortical thinning throughout the lifespan. *Sci. Rep.* **10**, 21803 (2020).
43. Burggren, A. C. *et al.* Reduced cortical thickness in hippocampal subregions among cognitively normal apolipoprotein E e4 carriers. *NeuroImage* **41**, 1177–1183 (2008).
44. Moon, H. S. *et al.* Contribution of Excitatory and Inhibitory Neuronal Activity to BOLD fMRI. *Cereb. Cortex N. Y. NY* **31**, 4053–4067 (2021).
45. Micheva, K. D. *et al.* A large fraction of neocortical myelin ensheathes axons of local inhibitory neurons. *eLife* **5**, e15784 (2016).
46. Stedehouder, J. *et al.* Local axonal morphology guides the topography of interneuron myelination in mouse and human neocortex. *eLife* **8**, e48615 (2019).
47. Stedehouder, J. *et al.* Fast-spiking Parvalbumin Interneurons are Frequently Myelinated

in the Cerebral Cortex of Mice and Humans. *Cereb. Cortex* **27**, 5001–5013 (2017).

48. Ahn, J. H. *et al.* Immunoreactivities of calbindin-D28k, calretinin and parvalbumin in the somatosensory cortex of rodents during normal aging. *Mol. Med. Rep.* **16**, 7191–7198 (2017).
49. Ueno, H. *et al.* Age-dependent and region-specific alteration of parvalbumin neurons and perineuronal nets in the mouse cerebral cortex. *Neurochem. Int.* **112**, 59–70 (2018).
50. Ueno, H. *et al.* Alteration of parvalbumin expression and perineuronal nets formation in the cerebral cortex of aged mice. *Mol. Cell. Neurosci.* **95**, 31–42 (2019).
51. Karetko-Sysa, M., Skangiel-Kramska, J. & Nowicka, D. Aging somatosensory cortex displays increased density of WFA-binding perineuronal nets associated with GAD-negative neurons. *Neuroscience* **277**, 734–746 (2014).
52. Peters, A. The effects of normal aging on myelin and nerve fibers: a review. *J. Neurocytol.* **31**, 581–593 (2002).
53. Northall, A. *et al.* Multimodal layer modelling reveals in vivo pathology in amyotrophic lateral sclerosis. *Brain* awad351 (2023) doi:10.1093/brain/awad351.
54. Blumenstock, S. *et al.* Cortical circuit dysfunction in a mouse model of alpha-synucleinopathy in vivo. *Brain Commun.* **3**, fcab273 (2021).
55. Kenkhuis, B. *et al.* 7T MRI allows detection of disturbed cortical lamination of the medial temporal lobe in patients with Alzheimer's disease. *NeuroImage Clin.* **21**, 101665 (2019).
56. Romito-DiGiacomo, R. R., Menegay, H., Cicero, S. A. & Herrup, K. Effects of Alzheimer's Disease on Different Cortical Layers: The Role of Intrinsic Differences in Aβ Susceptibility. *J. Neurosci.* **27**, 8496–8504 (2007).
57. Batiuk, M. Y. *et al.* Upper cortical layer–driven network impairment in schizophrenia. *Sci. Adv.* **8**, eabn8367.
58. Wagstyl, K. *et al.* Multiple markers of cortical morphology reveal evidence of supragranular thinning in schizophrenia. *Transl. Psychiatry* **6**, e780–e780 (2016).

59. McColgan, P., Joubert, J., Tabrizi, S. J. & Rees, G. The human motor cortex microcircuit: insights for neurodegenerative disease. *Nat. Rev. Neurosci.* **21**, 401–415 (2020).

60. Schirmer, L. *et al.* Neuronal vulnerability and multilineage diversity in multiple sclerosis. *Nature* **573**, 75–82 (2019).

61. Clements, R. J., McDonough, J. & Freeman, E. J. Distribution of parvalbumin and calretinin immunoreactive interneurons in motor cortex from multiple sclerosis post-mortem tissue. *Exp. Brain Res.* **187**, 459–465 (2008).

62. Falco, A., Pennucci, R., Brambilla, E. & de Curtis, I. Reduction in parvalbumin-positive interneurons and inhibitory input in the cortex of mice with experimental autoimmune encephalomyelitis. *Exp. Brain Res.* **232**, 2439–2449 (2014).

63. Dubey, M. *et al.* Myelination synchronizes cortical oscillations by consolidating parvalbumin-mediated phasic inhibition. *eLife* **11**, e73827 (2022).

64. Yang, W., Williams, A. & Sun, Q.-Q. Circuit Mechanisms Underlying Epileptogenesis in a Mouse Model of Focal Cortical Malformation. *Curr. Biol.* **31**, 334-345.e4 (2021).

65. Dachet, F. *et al.* Predicting novel histopathological microlesions in human epileptic brain through transcriptional clustering. *Brain* **138**, 356–370 (2015).

66. Reeves, C. *et al.* Combined Ex Vivo 9.4T MRI and Quantitative Histopathological Study in Normal and Pathological Neocortical Resections in Focal Epilepsy. *Brain Pathol. Zurich Switz.* **26**, 319–333 (2016).

67. Oldfield, R. C. The assessment and analysis of handedness: The Edinburgh inventory. *Neuropsychologia* **9**, 97–113 (1971).

68. Elbert, T., Pantev, C., Wienbruch, C., Rockstroh, B. & Taub, E. Increased Cortical Representation of the Fingers of the Left Hand in String Players. *Science* **270**, 305–307 (1995).

69. Ragert, P., Schmidt, A., Altenmüller, E. & Dinse, H. R. Superior tactile performance and learning in professional pianists: evidence for meta-plasticity in musicians: Meta-plasticity in musicians. *Eur. J. Neurosci.* **19**, 473–478 (2004).

70. Schwenkreis, P. *et al.* Assessment of sensorimotor cortical representation asymmetries and motor skills in violin players: Sensorimotor asymmetries in violin players. *Eur. J. Neurosci.* **26**, 3291–3302 (2007).

71. Nasreddine, Z. S. *et al.* The Montreal Cognitive Assessment, MoCA: A Brief Screening Tool For Mild Cognitive Impairment. *J. Am. Geriatr. Soc.* **53**, 695–699 (2005).

72. Marques, J. P. *et al.* MP2RAGE, a self bias-field corrected sequence for improved segmentation and T1-mapping at high field. *NeuroImage* **49**, 1271–1281 (2010).

73. Haacke, E. M., Xu, Y., Cheng, Y.-C. N. & Reichenbach, J. R. Susceptibility weighted imaging (SWI). *Magn. Reson. Med.* **52**, 612–618 (2004).

74. Schweisfurth, M. A., Schweizer, R. & Frahm, J. Functional MRI indicates consistent intra-digit topographic maps in the little but not the index finger within the human primary somatosensory cortex. *NeuroImage* **56**, 2138–2143 (2011).

75. Schweisfurth, M. A., Frahm, J. & Schweizer, R. Individual left-hand and right-hand intra-digit representations in human primary somatosensory cortex. *Eur. J. Neurosci.* **42**, 2155–2163 (2015).

76. Schweisfurth, M. A., Schweizer, R. & Treue, S. Feature-based attentional modulation of orientation perception in somatosensation. *Front. Hum. Neurosci.* **8**, (2014).

77. Schweizer, R., Voit, D. & Frahm, J. Finger representations in human primary somatosensory cortex as revealed by high-resolution functional MRI of tactile stimulation. *NeuroImage* **42**, 28–35 (2008).

78. Dale, A. M., Fischl, B. & Sereno, M. I. Cortical Surface-Based Analysis. 16 (1999).

79. Fischl, B., Sereno, M. I. & Dale, A. M. Cortical Surface-Based Analysis. 13 (1999).

80. Acosta-Cabronero, J. *et al.* A robust multi-scale approach to quantitative susceptibility mapping. *NeuroImage* **183**, 7–24 (2018).

81. Avants, B. B. *et al.* A reproducible evaluation of ANTs similarity metric performance in brain image registration. *NeuroImage* **54**, 2033–2044 (2011).

82. Bazin, P.-L. & Pham, D. L. Topology-Preserving Tissue Classification of Magnetic Resonance Brain Images. *IEEE Trans. Med. Imaging* **26**, 487–496 (2007).

83. Han, X. *et al.* CRUISE: Cortical reconstruction using implicit surface evolution. *NeuroImage* **23**, 997–1012 (2004).

84. Sethian, J. A. *Level set methods and fast marching methods: evolving interfaces in computational geometry, fluid mechanics, computer vision, and materials science*. vol. 3 (Cambridge university press, 1999).

85. Waehnert, M. D. *et al.* Anatomically motivated modeling of cortical laminae. *NeuroImage* **93**, 210–220 (2014).

86. Waehnert, M. D. *et al.* A subject-specific framework for in vivo myeloarchitectonic analysis using high resolution quantitative MRI. *NeuroImage* **125**, 94–107 (2016).

87. Aggarwal, M., Li, X., Gröhn, O. & Sierra, A. Nuclei-specific deposits of iron and calcium in the rat thalamus after status epilepticus revealed with quantitative susceptibility mapping (QSM). *J. Magn. Reson. Imaging JMRI* **47**, 554–564 (2018).

88. Deh, K. *et al.* Magnetic susceptibility increases as diamagnetic molecules breakdown: Myelin digestion during multiple sclerosis lesion formation contributes to increase on QSM. *J. Magn. Reson. Imaging* **48**, 1281–1287 (2018).

89. Lorio, S. *et al.* Quantitative MRI susceptibility mapping reveals cortical signatures of changes in iron, calcium and zinc in malformations of cortical development in children with drug-resistant epilepsy. *NeuroImage* **238**, 118102 (2021).

90. Wang, Y. & Liu, T. Quantitative susceptibility mapping (QSM): Decoding MRI data for a tissue magnetic biomarker. *Magn. Reson. Med.* **73**, 82–101 (2015).

91. Tosun, D. *et al.* Cortical surface segmentation and mapping. *NeuroImage* **23**, S108–S118 (2004).

92. O'Brien, K. R. *et al.* Robust T1-Weighted Structural Brain Imaging and Morphometry at 7T Using MP2RAGE. *PLoS ONE* **9**, e99676 (2014).

93. Hoopes, A., Mora, J. S., Dalca, A. V., Fischl, B. & Hoffmann, M. SynthStrip: skull-stripping for any brain image. *NeuroImage* **260**, 119474 (2022).

94. Geyer, S., Schleicher, A. & Zilles, K. Areas 3a, 3b, and 1 of Human Primary Somatosensory Cortex: 1. Microstructural Organization and Interindividual Variability.

NeuroImage **10**, 63–83 (1999).

95. Yousry, T. A. *et al.* Localization of the motor hand area to a knob on the precentral gyrus. A new landmark. *Brain* **120**, 141–157 (1997).
96. Glasser, M. F. *et al.* A multi-modal parcellation of human cerebral cortex. *Nature* **536**, 171–178 (2016).
97. Glasser, M. F. & Van Essen, D. C. Mapping Human Cortical Areas *In Vivo* Based on Myelin Content as Revealed by T1- and T2-Weighted MRI. *J. Neurosci.* **31**, 11597–11616 (2011).
98. Sereno, M. I., Sood, M. R. & Huang, R.-S. Topological Maps and Brain Computations From Low to High. *Front. Syst. Neurosci.* **16**, 787737 (2022).
99. In, M.-H., Posnansky, O. & Speck, O. PSF mapping-based correction of eddy-current-induced distortions in diffusion-weighted echo-planar imaging: Correction of Distortions in DW-EPI. *Magn. Reson. Med.* **75**, 2055–2063 (2016).
100. Kuehn, E., Haggard, P., Villringer, A., Pleger, B. & Sereno, M. I. Visually-Driven Maps in Area 3b. *J. Neurosci.* **38**, 1295–1310 (2018).
101. Stringer, E. A. *et al.* Distinct fine-scale fMRI activation patterns of contra- and ipsilateral somatosensory areas 3b and 1 in humans: Tactile Response in Human S1 Cortex. *Hum. Brain Mapp.* **35**, 4841–4857 (2014).
102. Puckett, A. M., Bollmann, S., Junday, K., Barth, M. & Cunnington, R. Bayesian population receptive field modeling in human somatosensory cortex. *NeuroImage* **208**, 116465 (2020).
103. Zeidman, P., Silson, E. H., Schwarzkopf, D. S., Baker, C. I. & Penny, W. Bayesian population receptive field modelling. *NeuroImage* **180**, 173–187 (2018).
104. Morgan, C. & Schwarzkopf, S. Comparison of human population receptive field estimates between scanners and the effect of temporal filtering. *F1000Research* **8**, (2020).
105. Urale, P. W. B., Puckett, A. M., York, A., Arnold, D. & Schwarzkopf, D. S. Highly accurate retinotopic maps of the physiological blind spot in human visual cortex. *Hum.*

Brain Mapp. hbm.25996 (2022) doi:10.1002/hbm.25996.

106. Spearman, C. Correlation calculated from faulty data. *Br. J. Psychol.* **1904–1920**, 271–295 (1910).
107. Hagler, D. J., Saygin, A. P. & Sereno, M. I. Smoothing and cluster thresholding for cortical surface-based group analysis of fMRI data. *NeuroImage* **33**, 1093–1103 (2006).
108. Kelley, D. J. *et al.* Automatic Physiological Waveform Processing for fMRI Noise Correction and Analysis. *PLOS ONE* **3**, e1751 (2008).
109. Glover, G. H., Li, T.-Q. & Ress, D. Image-based method for retrospective correction of physiological motion effects in fMRI: RETROICOR. *Magn. Reson. Med.* **44**, 162–167 (2000).
110. Birn, R. M., Diamond, J. B., Smith, M. A. & Bandettini, P. A. Separating respiratory-variation-related fluctuations from neuronal-activity-related fluctuations in fMRI. *NeuroImage* **31**, 1536–1548 (2006).
111. Lohmann, G. *et al.* Lipsia—a new software system for the evaluation of functional magnetic resonance images of the human brain. *Comput. Med. Imaging Graph.* **25**, 449–457 (2001).
112. Lohmann, G., Loktyushin, A., Stelzer, J. & Scheffler, K. Eigenvector centrality mapping for ultrahigh resolution fMRI data of the human brain. 494732 Preprint at https://doi.org/10.1101/494732 (2018).
113. Sullivan, C. & Kaszynski, A. PyVista: 3D plotting and mesh analysis through a streamlined interface for the Visualization Toolkit (VTK). *J. Open Source Softw.* **4**, 1450 (2019).
114. Root, V. *et al.* Complex pattern of facial remapping in somatosensory cortex following congenital but not acquired hand loss. *eLife* **11**, e76158 (2022).
115. Janssen, A. Studentized permutation tests for non-i.i.d. hypotheses and the generalized Behrens-Fisher problem. *Stat. Probab. Lett.* **36**, 9–21 (1997).
116. Noguchi, K., Konietschke, F., Marmolejo-Ramos, F. & Pauly, M. Permutation tests are robust and powerful at 0.5% and 5% significance levels. *Behav. Res. Methods* **53**,

2712–2724 (2021).

117. Kherad-Pajouh, S. & Renaud, O. A general permutation approach for analyzing repeated measures ANOVA and mixed-model designs. *Stat. Pap.* **56**, 947–967 (2015).

118. Efron, B. & Tibshirani, R. *An introduction to the bootstrap*. (Chapman & Hall, 1993).

119. Heo, I., Veen, D. & Van de Schoot, R. Tutorial: JASP for Bayesian analyses with default priors. (2020) doi:10.5281/zenodo.4008339.

120. Pfadt, J. M., Bergh, D. van den, Sijtsma, K. & Wagenmakers, E.-J. A tutorial on Bayesian single-test reliability analysis with JASP. *Behav. Res. Methods* **55**, 1069–1078 (2023).

121. Van Doorn, J. *et al.* The JASP guidelines for conducting and reporting a Bayesian analysis. *Psychon. Bull. Rev.* **28**, 813–826 (2021).

122. Mücke, M. *et al.* [Quantitative sensory testing]. *Schmerz Berl. Ger.* **28**, 635–646; quiz 647–648 (2014).

123. Brainard, D. H. The Psychophysics Toolbox. *Spat. Vis.* **10**, 433–436 (1997).

124. Pelli, D. G. The VideoToolbox software for visual psychophysics: transforming numbers into movies. *Spat. Vis.* **10**, 437–442 (1997).

125. Gescheider, G. A., Zwislocki, J. J. & Rasmussen, A. Effects of stimulus duration on the amplitude difference limen for vibrotaction. *J. Acoust. Soc. Am.* **100**, 2312–2319 (1996).

126. Thornbury, J. M. & Mistretta, C. M. Tactile Sensitivity as a Function of Age1. *J. Gerontol.* **36**, 34–39 (1981).

127. Cornsweet, T. N. The Staircase-Method in Psychophysics. *Am. J. Psychol.* **75**, 485–491 (1962).

128. Wu, J. Z., Dong, R. G., Smutz, W. P. & Rakheja, S. Dynamic interaction between a fingerpad and a flat surface: experiments and analysis. *Med. Eng. Phys.* **25**, 397–406 (2003).

129. Kingdom, F. A. A. & Prins, N. *Psychophysics: A Practical Introduction*. (Academic Press, 2016).

130. McNicol, D. *A Primer of Signal Detection Theory*. (Psychology Press, 2005).

131. Kalisch, T., Tegenthoff, M. & Hubert, D. R. Improvement of sensorimotor functions in old age by passive sensory stimulation. *Clin. Interv. Aging* **Volume 3**, 673–690 (2008).

132. Kuehn, E., Doehler, J. & Pleger, B. The influence of vision on tactile Hebbian learning. *Sci. Rep.* **7**, 9069 (2017).

133. Cardini, F. *et al.* Viewing One's Own Face Being Touched Modulates Tactile Perception: An fMRI Study. *J. Cogn. Neurosci.* **23**, 503–513 (2011).

134. Cardini, F., Longo, M. R., Driver, J. & Haggard, P. Rapid enhancement of touch from non-informative vision of the hand. *Neuropsychologia* **50**, 1954–1960 (2012).

135. Kalisch, T., Ragert, P., Schwenkreis, P., Dinse, H. R. & Tegenthoff, M. Impaired Tactile Acuity in Old Age Is Accompanied by Enlarged Hand Representations in Somatosensory Cortex. *Cereb. Cortex* **19**, 1530–1538 (2009).

136. Pleger, B. *et al.* Shifts in cortical representations predict human discrimination improvement. *Proc. Natl. Acad. Sci.* **98**, 12255–12260 (2001).

137. Vieluf, S., Godde, B., Reuter, E.-M. & Voelcker-Rehage, C. Age-related differences in finger force control are characterized by reduced force production. *Exp. Brain Res.* **224**, 107–117 (2013).

138. Voelcker-Rehage, C. & Alberts, J. L. Age-related changes in grasping force modulation. *Exp. Brain Res.* **166**, 61–70 (2005).

139. Gryga, M. *et al.* Bidirectional gray matter changes after complex motor skill learning. *Front. Syst. Neurosci.* **6**, (2012).

140. National Research Council (US) Committee for the Update of the Guide for theCare and Use of Laboratory Animals. *Guide for the Care and Use of Laboratory Animals*. (National Academies Press (US), 2011).

141. Pachitariu, M. *et al.* Suite2p: beyond 10,000 neurons with standard two-photon microscopy. 061507 Preprint at https://doi.org/10.1101/061507 (2017).

142. Keemink, S. W. *et al.* FISSA: A neuropil decontamination toolbox for calcium imaging signals. *Sci. Rep.* **8**, 3493 (2018).

143. Schindelin, J. *et al.* Fiji: an open-source platform for biological-image analysis. *Nat.*